RESEARCH ARTICLE

On Finite-Time Anti-Saturated Proximity Control with a Tumbling Non-Cooperative Space Target

Caisheng Wei[1], Yang Li[1], Zeyang Yin[1*], Liang Zhou[2], and Jinglang Feng[3]

[1]School of Automation, Central South University, Changsha, China. [2]Intelligent Science & Technology Academy Limited of CASIC, Beijing, China. [3]Department of Mechanical and Aerospace Engineering, University of Strathclyde, Glasgow, UK.

*Address correspondence to: yinzeyang@csu.edu.cn

For the challenging problem that a spacecraft approaches a tumbling target with non-cooperative maneuver, an anti-saturated proximity control method is proposed in this paper. First, a brand-new appointed-time convergent performance function is developed via exploring Bézier curve to quantitatively characterize the transient and steady-state behaviors of the pose tracking error system. The major advantage of the proposed function is that the actuator saturation phenomenon at the beginning can be effectively reduced. Then, an anti-saturated pose tracking controller is devised along with an adaptive saturation compensator. Wherein, the finite-time stability of both the pose and its velocity error signals are guaranteed simultaneously in the presence of actuator saturation. Finally, 2 groups of illustrative examples are organized and verify that the close-range proximity is effectively realized even with unknown target maneuver.

Introduction

The past few decades have witnessed the burgeoning development of on-orbit servicing in light of various meaningful space applications such as repair of malfunctioning satellites, debris removal, on-orbit assembly, and so on [1–4]. As for the orbit-servicing targets, they are usually divided into 2 categories, i.e., cooperative and non-cooperative ones, based on whether the space targets have active cross-link communication and cooperative identifiers with the servicing spacecraft or not. Before executing the orbit-servicing task, close-range rendezvous and proximity is an inevitable process in which precise observation for the orbit-servicing target is implemented to determine the docking ports and time (for the cooperative target) or capture ports and time (for the non-cooperative target) [5]. Thus, highly reliable and precise rendezvous and proximity control methods are essential to guarantee the safety and success of the on-orbit servicing task [6,7].

Based on the above discussions, there are many rendezvous and proximity control methods proposed in the existing works. For example, a robust H_∞ control method was investigated for spacecraft rendezvous problem via using Clohessy–Wiltshire equations to describe the relative motion dynamics between 2 spacecrafts in [8]. A robust model predictive control (MPC) scheme was devised to solve the problem of spacecraft rendezvous based on the Hill–Clohessy–Wiltshire model in the presence of additive disturbances in [9]. Owing to the effectiveness of MPC in coping with the state constraints, MPC-based rendezvous law was further investigated in [10]. Moreover, in light of the high robustness and low sensitivity to the uncertainties and disturbances, sliding mode control (SMC)-based rendezvous and proximity methods have attracted considerable attention such as in [11,12] and references therein. Although effective

to solve the rendezvous problem with a cooperative target, the abovementioned control methods are seriously dependent on the information shared between the spacecrafts in the target's reference frame. Once the target is non-cooperative, the orbit and attitude information cannot be known by the servicing spacecraft. In this case, the foregoing corresponding control methods are inadequate obviously to the non-cooperative target.

To solve the abovementioned defects existing in the rendezvous control methods for cooperative targets, many attempts have been made to handle the relative motion tracking problem for non-cooperative targets. With consideration of the loss of target's orbit information, line of sight (LOS) frame established in the servicing spacecraft was proposed in view of the easy access of relative distance (by laser radar or angle-only navigation algorithm [13,14]) and LOS direction information from the navigation devices [15]. Based on the LOS coordinate frame, a fixed-time fault-tolerant controller was devised for the spacecraft rendezvous and docking with a freely tumbling target via exploring the SMC technique in [16]. Moreover, with consideration of the target's active maneuver, an adaptive SMC-based motion tracking control law was presented in [17]. In practice, actuator saturation is often encountered, which will degrade the control performance and even cause the system instability [18]. To guarantee the stability and safety of the final phase proximity operations with a non-cooperative target, a saturated control law was developed to solve the motion tracking problem with consideration of the path constraints and actuator magnitude constraints in [19]. An adaptive passivity-based SMC method was proposed for LOS rendezvous considering the input saturation problem [20]. Although there are various effective motion tracking control methods presented in the existing works, how to ensure the high-quality tracking

performance behaviors (including the transient and steady-state behaviors) is still an open issue and an interesting field for the on-orbit servicing task.

A particular quantitative performance bound technique, prescribed performance control (PPC), was proposed by Bechlioulis and Rovithakis [21] and then has attracted wide attention in the control system design for robotic manipulators, unmanned surface vehicles, and vehicle suspensions [22–26]. Due to its unique advantage in quantitatively characterizing and synthesizing the transient and steady-state tracking performance, PPC was adopted to develop stable attitude controllers for single or multiple spacecraft in [27–29]. Moreover, the spatial motion constraints during the spacecraft proximity operations were approximated by 2 performance functions in the PPC structure. In addition, an effective pose controller was designed to guarantee the motion tracking performance for spacecraft rendezvous in [30]. To further accelerate the convergence rate, finite-time or appointed-time PPC methods have been proposed in the existing works [31–34]. For example, an appointed-time PPC was proposed for the spacecraft rendezvous orbit and attitude control in [35]. By the user's specific choice for the parameters of the performance function, the finite-time or appointed-time convergence can be achieved for the controlled systems.

However, a major defect in the aforementioned PPC control methods should be considered in practical engineering, that is, the actuator saturation induced by high sensitivity to the performance bounds. When the system state reaches the performance bound, the transformed state will be pretty large, which easily causes the actuator saturation [36]. One of the reasons that the relevant PPC control is sensitive to the performance bound is that the initial derivative of the performance function is nonzero and often very large. This forces the controlled system state change very fast and easily leads to a very large control input signal exceeding the actuator saturation bound. Although the saturation problem can be eased by constructing a compensation controller with an auxiliary system [37], nonsmooth change of the system states will cause quite a lot of fuel consumption, which is not permitted in many practical applications including the on-orbit servicing tasks.

Inspired by the foregoing observations, this paper tries to propose a brand-new anti-saturated appointed-time pose tracking control method for spacecraft rendezvous with a tumbling non-cooperative target. Compared with the existing works, the contributions of our work are 2-fold:

• A novel appointed-time convergent performance function is developed via exploring Bézier curve. Compared with existing performance functions in [21–23,25,26,32], the initial derivative of the proposed one is zero, and the transient behaviors can be tuned intuitively by the users. This is the first way to reduce the actuator saturation during the close-range proximity operations.

• Based on the devised performance function, an anti-saturated pose tracking controller is developed with an adaptive saturation compensator. Compared with the traditional finite-time control methods, the tedious discontinuous fractional type of finite-time controllers in the existing works is avoided, while the finite-time convergence of both the pose and its derivatives signals is achieved simultaneously.

The remainder of this paper is organized as follows. Relative Motion Dynamics shows the problem statement with description of the relative motion dynamics during the close-range proximity operations. An anti-saturated appointed-time pose tracking

controller is devised in Methods and Results along with stability analysis. Illustrative simulations of the proposed control method are organized in Numerical Simulations and Discussions, and some conclusions are drawn in Conclusion.

Notations: $\top$, $\|\bullet\|$, $|\bullet|$, $\sigma(\bullet)$ are the vector transpose, the Euclidean norm of a vector, the absolute value of a real number, and the eigenvalue of a nonsingular matrix, respectively. $\mathbb{R}^n$, $\mathbb{R}^{n+}$ represent the set of n-dimensional real numbers and n-dimensional positive real numbers, respectively. $\mathbb{N}$, $\mathbb{N}^+$ denote the set of non-negative integers and positive integers, respectively.

Relative Motion Dynamics

Before moving, it is assumed that 2 spacecrafts are in orbit around the earth. Wherein, one is the servicing spacecraft (chaser for brevity), which has the control ability to approach the target. The other is the target spacecraft (target for brevity), which is tumbling and has no active interaction with the chaser. To develop the subsequent relative motion dynamics, the following coordinate frames are defined. $\mathcal{F}_I: O_I X_I Y_I Z_I$ represents the Earth-centered inertial frame with the origin O_I being located in the earth center of mass and axes $O_I X_I$, $O_I Z_I$ pointing to the spring equinox and north pole, respectively. Employing a right-hand coordinate system can generate $O_I Y_I$. $\mathcal{F}_s: O_c X_s Y_s Z_s$ denotes the LOS coordinate system with the origin O_c being the mass center of the target. Axis $O_c X_s$ is the sight direction of chaser, which is pointed to the target. Axis $O_c Y_s$ is vertical to the longitudinal plane containing axis $O_c X_s$. Axis $O_c Z_s$ is generated by applying the right-hand coordinate system. $\mathcal{F}_{bt}: O_t X_t Y_t Z_t$ and $\mathcal{F}_{bc}: O_c X_c Y_c Z_c$ are, respectively, the body-fixed frames of the target and the chaser.

Relative translational motion

As Fig. 1 shows, the relative translational motion between the chaser and target is described in the LOS coordinate frame [17,38]:

$$\begin{cases} \ddot{r} - r\left(\dot{q}_\epsilon^2 + \dot{q}_\beta^2 \cos^2 q_\epsilon\right) = a_{tx} + d_x - u_{cx} \\ \qquad r\ddot{q}_\epsilon + 2\dot{r}\dot{q}_\epsilon + r\dot{q}_\beta^2 \sin q_\epsilon \cos q_\epsilon = a_{ty} + d_y - u_{cy} \\ -r\ddot{q}_\beta \cos q_\epsilon + 2r\dot{q}_\beta \dot{q}_\epsilon \sin q_\epsilon - 2\dot{r}\dot{q}_\beta \cos q_\epsilon = a_{tz} + d_z - u_{cz} \end{cases} \quad (1)$$

where r, q_ϵ, $q_\beta \in \mathbb{R}$ denote the distance between the chaser and the target, the elevation angle, and azimuth angle in the LOS coordinate frame, respectively. Moreover, as Fig. 1 shows, The initial elevation and azimuth angles satisfy $q_\epsilon \in (-\pi/2, \pi/2)$, $q_\beta \in (-\pi, \pi)$. $\boldsymbol{a}_t = [a_{tx}, a_{ty}, a_{tz}]^\top \in \mathbb{R}^3$ is the accelerated velocity of the tumbling target, which is unknown for the chaser. $\boldsymbol{d} = [d_x, d_y, d_z]^\top \in \mathbb{R}^3$ represents the unknown space perturbations. $\boldsymbol{u}_c = [u_{cx}, u_{cy}, u_{cz}]^\top \in \mathbb{R}^3$ is the accelerated velocity of the chaser to be designed.

Without loss of generality, the final relative distance is supposed to be $r_d > 0$. When the non-cooperative target is tumbling, the position of the feature point on the target will be changed. Consequently, the desired orbital information will be changed. It is assumed that the unit vector of the feature point in the body-fixed coordinate is defined as $\boldsymbol{n}_b$, and then the desired LOS orientation is $-\boldsymbol{n}_b$. The projection of the desired LOS orientation in the inertial frame $\mathcal{F}_I$ is:

$$\boldsymbol{\rho}_I = \boldsymbol{C}_I^{bt}\left(-\boldsymbol{n}_b r_d\right) = \left[X_I, Y_I, Z_I\right]^\top, \quad (2)$$

where C_I^{bt} denotes the direction cosine matrix from the body-fixed frame $\mathcal{F}_{bt}$ of the target to the inertial frame $\mathcal{F}_I$. With consideration of the transformation from the LOS frame $\mathcal{F}_s$ to the inertial frame $\mathcal{F}_I$, vector ρ_I also equals to

$$\rho_I = C_I^s \rho_s = C_I^s [r_d, 0, 0]^\top, \quad (3)$$

where ρ_s is the vector defined in the LOS frame $\mathcal{F}_s$. Direction cosine matrix C_s^I is defined as

$$C_s^I = [C_I^s]^\top = \begin{bmatrix} \cos q_\varepsilon \cos q_\beta & \sin q_\varepsilon & -\cos q_\varepsilon \sin q_\beta \\ -\sin q_\varepsilon \cos q_\beta & \cos q_\varepsilon & \sin q_\varepsilon \sin q_\beta \\ \sin q_\varepsilon & 0 & \cos q_\beta \end{bmatrix} \quad (4)$$

Accordingly, the desired LOS distance, elevation angle, and azimuth angle $\rho_d = [r_d, q_{\varepsilon d}, q_{\beta d}]^\top$ and their time derivatives can be calculated by the foregoing 2 equations. By defining the translational motion tracking errors $r_e = r - r_d$, $q_{\varepsilon e} = q_\varepsilon - q_{\varepsilon d}$, and $q_{\beta e} = q_\beta - q_{\beta d}$, one can obtain the tracking error system for the relative translational motion, i.e.,

$$\begin{cases} \dot{s}_1 = s_2 \\ \dot{s}_2 = f_o + g_o (a_t + d - u_c), \end{cases} \quad (5)$$

where $s_1 = [r_e, q_{\varepsilon e}, q_{\beta e}]^\top$ and $\dot{s}_1 = s_1 = [\dot{r}_e, \dot{q}_{\varepsilon e}, \dot{q}_{\beta e}]^\top$. Nonlinear functions f_o and g_o are expressed by

$$\begin{cases} f_o = \begin{bmatrix} r(\dot{q}_\varepsilon^2 + \dot{q}_\beta^2 \cos^2 q_\varepsilon) + \ddot{r}_d \\ -2\dot{r}\dot{q}_\varepsilon / r - \dot{q}_\beta^2 \sin q_\varepsilon \cos q_\varepsilon + \ddot{q}_{\varepsilon d} \\ 2\dot{q}_\beta \dot{q}_\varepsilon \tan q_\varepsilon - 2\dot{r}\dot{q}_\beta / r + \ddot{q}_{\beta d} \end{bmatrix} \\ g_o = \text{diag}\{1, 1/r, -1/(r\cos q_\varepsilon)\}. \end{cases} \quad (6)$$
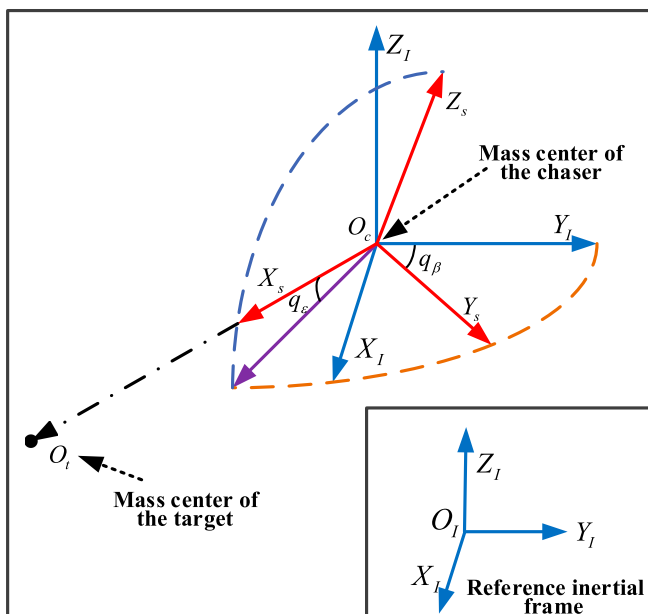

Fig. 1. Sketch of the LOS coordinate frame.

Relative rotational motion

In the foregoing subsection, the relative translational motion dynamics between the chaser and target have been established. In this part, the relative rotational motion dynamics will be given. First, we apply the quaternion to describe the attitude motion for nonsingular attitude representation. The kinematics and dynamics of the chaser attitude are given by [39,40] as

$$\begin{cases} \dot{\varrho}_c = \frac{1}{2} A(\varrho_c) \omega_c \\ J_c \dot{\omega}_c = -\omega_c^\times J_c \omega_c + \tau_c + \tau_d, \end{cases} \quad (7)$$

where $\varrho_c = [\varrho_{cv}, \varrho_{c4}]^\top$ is the unit quaternion for the attitude representation, which satisfies $\varrho_{cv}^\top \varrho_{cv} + \varrho_{c4}^2 = 1$. ω_c denotes the angle velocity of the chaser. J_c is the uncertain inertia matrix, which is uncertain due to the fuel consumption and system uncertainties. τ_c is the control torque to be designed. τ_d is the space perturbations, which are unknown but bounded. Matrix $A(\varrho_c)$ equals to

$$A(\varrho_c) = \begin{bmatrix} A_v(\varrho_c) \\ A_4(\varrho_c) \end{bmatrix} = \begin{bmatrix} \varrho_{c4} I_3 + \varrho_{cv}^\times \\ -\varrho_{cv}^\top \end{bmatrix}$$

To facilitate the subsequent attitude controller design, the desired attitude command of the chaser should be preplanned. First, we assume that the measuring sensors and solar panels are installed on the X_c and Y_c-axes of the body-fixed frame $\mathcal{F}_{bc}$, respectively. To ensure the effective observing and monitoring for the non-cooperative target, the center axes of the measure sensors should be along with the vector x_{bcd} to be given later. Moreover, to obtain more solar energy, the solar panels should be vertical with the solar ray. The solar ray represented in the inertial frame $\mathcal{F}_I$ is denoted as $\zeta \in \mathbb{R}^3$. Then, in the body-fixed frame $\mathcal{F}_{bc}$ of the chaser, the desired triaxial unit vector for the chaser is defined as

$$\begin{cases} x_{bcd} = \dfrac{\rho_I}{r_d} \\ y_{bcd} = \dfrac{\rho_I^\times \zeta}{\|\rho_I^\times \zeta\|} \\ z_{bcd} = x_{bcd}^\times y_{bcd}. \end{cases} \quad (8)$$

Based on the above equation, the translational matrix from the initial frame $\mathcal{F}_I$ to the desired body-fixed frame $\mathcal{F}_{cd}$ of the chaser is expressed by

$$C_{cd}^I = [x_{bcd}, y_{bcd}, z_{bcd}]^\top \in \mathbb{R}^{3\times 3}. \quad (9)$$

The desired attitude command in quaternion $\varrho_{cd} = [\varrho_{cdv}^\top, \varrho_{cd4}]^\top$ can be computed by solving the following equation

$$C_{cd}^I = (\varrho_{cd4}^2 - \varrho_{cdv}^\top \varrho_{cdv}) I_3 + 2\varrho_{cdv}\varrho_{cdv}^\top - 2\varrho_{cd4}[\varrho_{cdv}^\times]. \quad (10)$$

Accordingly, the attitude tracking error vector of the chaser is defined as $\varrho_{ce} = \varrho_c \otimes \varrho_{cd}^{-1} = [\varrho_{cev}^\top, \varrho_{ce4}]^\top$ with $\varrho_{cd}^{-1} = [-\varrho_{cdv}^\top, \varrho_{cd4}]^\top$. The angle velocity tracking error vector is defined as $\omega_{ce} = \omega_c - C_c^{cd}\omega_{cd}$ with translational matrix $C_c^{cd} = (\varrho_{ce4}^2 - \varrho_{cev}^\top \varrho_{cev}) I_3 + 2\varrho_{cev}\varrho_{cev}^\top - 2\varrho_{ce4}\varrho_{cev}^\times$. Then, the attitude tracking error system in the proximity phase is obtained as

$$\begin{cases} \dot{\varrho}_{ce} & = \dfrac{1}{2}A(\varrho_{ce})\boldsymbol{\omega}_{ce} \\ \boldsymbol{J}_c\dot{\boldsymbol{\omega}}_{ce} = -\boldsymbol{\omega}_c^\times \boldsymbol{J}_c\boldsymbol{\omega}_c - \boldsymbol{J}_c\left(\boldsymbol{C}_c^{cd}\dot{\boldsymbol{\omega}}_{cd} - \boldsymbol{\omega}_{ce}^\times \boldsymbol{C}_c^{cd}\boldsymbol{\omega}_{cd}\right) + \boldsymbol{\tau}_c + \boldsymbol{\tau}_d. \end{cases} \quad (11)$$

Based on Eq. 11, by defining 2 new state variables $\boldsymbol{s}_3 = \boldsymbol{\varrho}_{cev}$, $\boldsymbol{s}_4 = \dot{\boldsymbol{s}}_3 = \dot{\boldsymbol{\varrho}}_{cev}$, a strict-feedback form for Eq. 11 is obtained as

$$\begin{cases} \dot{\boldsymbol{s}}_3 = \boldsymbol{s}_4 \\ \dot{\boldsymbol{s}}_4 = \boldsymbol{f}_a(\boldsymbol{\varrho}_{ce}, \dot{\boldsymbol{\varrho}}_{ce}) + \boldsymbol{g}_a(\boldsymbol{\varrho}_{ce})\boldsymbol{\tau}_c^* + \boldsymbol{\tau}_d^*, \end{cases} \quad (12)$$

with

$$\boldsymbol{f}_a(\boldsymbol{\varrho}_{ce}, \dot{\boldsymbol{\varrho}}_{ce}) = -\mathcal{M}^{-1}(\boldsymbol{\varrho}_{ce})\left[\boldsymbol{C}(\boldsymbol{\varrho}_{ce}, \dot{\boldsymbol{\varrho}}_{ce})\dot{\boldsymbol{\varrho}}_{cev} + \mathcal{G}(\boldsymbol{\varrho}_{ce})\right], \quad (13\text{A})$$

$$\boldsymbol{g}_a(\boldsymbol{\varrho}_{ce}) = \mathcal{M}^{-1}(\boldsymbol{\varrho}_{ce}), \quad (13\text{B})$$

$$\boldsymbol{\tau}_c^* = \boldsymbol{P}^\top \boldsymbol{\tau}_c, \quad (13\text{C})$$

$$\boldsymbol{\tau}_d^* = \boldsymbol{g}_a(\boldsymbol{\varrho}_{ce})\boldsymbol{P}^\top \boldsymbol{\tau}_d. \quad (13\text{D})$$

where matrix $\boldsymbol{P} = [A_v(\boldsymbol{\varrho}_{ce})/2]^{-1}$, $\mathcal{M}(\boldsymbol{\varrho}_{ce}) = \boldsymbol{P}^\top \boldsymbol{J}_c\boldsymbol{P}$, $\mathcal{G}(\boldsymbol{\varrho}_{ce}) = \boldsymbol{P}^\top(\boldsymbol{\omega}_c^\times \boldsymbol{J}_c\boldsymbol{\omega}_c - \boldsymbol{J}_c\boldsymbol{\omega}_{ce}^\times \boldsymbol{\omega}_c + \boldsymbol{J}_c\boldsymbol{C}_c^{cd}\dot{\boldsymbol{\omega}}_{cd})$, and $\boldsymbol{C}(\boldsymbol{\varrho}_{ce}, \dot{\boldsymbol{\varrho}}_{ce}) = -\mathcal{M}(\boldsymbol{\varrho}_{ce})\dot{\boldsymbol{P}}^{-1}\boldsymbol{P}$.

Based on Eqs. 5 and 12, by defining $\boldsymbol{\chi}_1 = \left[\boldsymbol{s}_1^\top, \boldsymbol{s}_3^\top\right]^\top$, $\boldsymbol{\chi}_2 = \dot{\boldsymbol{\chi}}_1 = \left[\boldsymbol{s}_2^\top, \boldsymbol{s}_4^\top\right]^\top \in \mathbb{R}^6$, the coupling relative translational and rotational motion dynamics under the actuator saturation are expressed by

$$\begin{cases} \dot{\boldsymbol{\chi}}_1 = \boldsymbol{\chi}_2 \\ \dot{\boldsymbol{\chi}}_2 = \boldsymbol{f}_1(\boldsymbol{\chi}_1, \boldsymbol{\chi}_2) + \boldsymbol{g}_1(\boldsymbol{\chi}_1, \boldsymbol{\chi}_2)\text{sat}(\boldsymbol{u}) + \boldsymbol{d}_1(\boldsymbol{\chi}_1, \boldsymbol{\chi}_2) \\ \quad = \boldsymbol{f}_1(\boldsymbol{\chi}_1, \boldsymbol{\chi}_2) + (\boldsymbol{g}_1(\boldsymbol{\chi}_1, \boldsymbol{\chi}_2) - 1)\text{sat}(\boldsymbol{u}) + \boldsymbol{d}_1(\boldsymbol{\chi}_1, \boldsymbol{\chi}_2) + \text{sat}(\boldsymbol{u}) \\ \quad = \boldsymbol{f}_1^*(\boldsymbol{\chi}_1, \boldsymbol{\chi}_2) + \text{sat}(\boldsymbol{u}), \end{cases} \quad (14)$$

where $\boldsymbol{f}_1^*(\boldsymbol{\chi}_1, \boldsymbol{\chi}_2) = \boldsymbol{f}_1(\boldsymbol{\chi}_1, \boldsymbol{\chi}_2) + (\boldsymbol{g}_1(\boldsymbol{\chi}_1, \boldsymbol{\chi}_2) - 1)\text{sat}(\boldsymbol{u}) + \boldsymbol{d}_1(\boldsymbol{\chi}_1, \boldsymbol{\chi}_2)$ with $\boldsymbol{f}_1(\boldsymbol{\chi}_1, \boldsymbol{\chi}_2) = \left[\boldsymbol{f}_o^\top, \boldsymbol{f}_a^\top\right]^\top \in \mathbb{R}^{6\times 6}$, $\boldsymbol{g}_1(\boldsymbol{\chi}_1, \boldsymbol{\chi}_2) = \text{diag}\{\boldsymbol{g}_o, \boldsymbol{g}_a\} \in \mathbb{R}^{6\times 6}$, $\boldsymbol{u} = \left[-\boldsymbol{u}_c^\top, \boldsymbol{\tau}_c^{*T}\right]^\top \in \mathbb{R}^6$, and $\boldsymbol{d}_1 = \left[\left(\boldsymbol{g}_o\boldsymbol{a}_t + \boldsymbol{g}_o\boldsymbol{d}\right)^\top, \boldsymbol{\tau}_d^{*T}\right]^\top \in \mathbb{R}^6$. $\text{sat}(\boldsymbol{u})$ is the output of the actuator and satisfies
w

$$\text{sat}(u_i) = \begin{cases} u_{i,\max}, & \text{if } u_i \geq u_{i,\max} \\ u_i, & \text{otherwise} \\ u_{i,\min}, & \text{if } u_i \leq u_{i,\max}, \end{cases} \quad (15)$$

where $u_{i,\max}$ and $u_{i,\min}$ are the relevant maximal and minimal saturation bounds of ith control input.

As presented in Eq. 14, the coupling nonlinear term $\boldsymbol{f}_1^*(\boldsymbol{\chi}_1, \boldsymbol{\chi}_2)$ is tedious and unknown. Based on the existing reference works [41,42], a radial basis neural network has been widely used to approximate the unknown nonlinearities. Without loss of generality, $\boldsymbol{f}_1^*(\boldsymbol{\chi}_1, \boldsymbol{\chi}_2) = \mathcal{W}^\top \boldsymbol{\varphi}(\boldsymbol{x})$ with $\mathcal{W} \in \mathbb{R}^{m\times 6}$ and $\boldsymbol{\varphi}(\boldsymbol{x}) \in \mathbb{R}^m$ being the optimal weight vector and Gaussian basis function, respectively (m is the number of hidden layer nodes, $\boldsymbol{x} = \left[\boldsymbol{\chi}_1^\top, \boldsymbol{\chi}_2^\top, \text{sat}^\top(\boldsymbol{u})\right]^\top$ is the input vector the radial

basis neural network). Note that the optimal weight vector $\mathcal{W}$ is unknown but bounded, which requires to estimate.

Based on the established relative motion dynamic model in Eq. 14, the control objectives of this paper are 2-fold: (a) The orbital and attitude tracking errors $\boldsymbol{\chi}_1$ and $\boldsymbol{\chi}_2$ can be steered by the designed controller to a small neighborhood around the origin with guaranteed performance within finite time. (b) The negative effects introduced by control saturation can be compensated by devising an adaptive antisaturation controller.

Methods

In this section, an adaptive anti-saturated appointed-time convergent controller will be developed for the tracking error system of the close-range proximity operations in Eq. 14.

Appointed-time convergent performance function with initial zero derivative via exploring Bézier curve

To guarantee the tracking performance and reduce the impact of the actuator saturation problem, a brand-new appointed-time convergent performance function is designed in this part.

To start, according to [43], suppose that there are $n + 1$ preassigned reference points in the 2-dimensional plane (the x-axes denotes time), i.e., $P_0(t_0, y_0)$, $P_1(t_1, y_1)$, …, $P_n(t_n, y_n)$. Then, the Bezier curve $B(\alpha)$ can be described as

$$\begin{cases} B(\alpha) = \beta_0(\alpha)P_0 + \beta_1(\alpha)P_1 + \cdots + \beta_n(\alpha)P_n \\ \beta_i(\alpha) = \dfrac{n!}{i!(n-i)!}\alpha^i(1-\alpha)^{n-i}, i = 0, 1, 2, \ldots, n \end{cases} \quad (16)$$

where $\alpha \in [0, 1]$ is a time-varying parameter. To guarantee the appointed-time convergence, the time series $t_0, t_1, t_2, \ldots, t_n$ satisfy $t_0 < t_1 < t_2 < t_n \leq T_a$ with T_a is appointed by the users. And then, parameter α is chosen as $\alpha = t/T_a$ which meets the requirement $\alpha \in [0, 1]$.

For the Bézier curve introduced in Eq. 16, there are 2 inherent properties [43] in the following:

Property 1. The Bézier curve $B(\alpha)$ will always go across and be tangent with the first and the final points $P_0(t_0, y_0)$, $P_n(t_n, y_n)$.

Property 2. The Bézier curve $B(\alpha)$ is always be trapped into the convex hull formulated by the chosen reference points $P_i(t_i, y_i)$ ($i = 0, 1, 2, \ldots, n$).

Based on the foregoing 2 properties, a corollary is obtained as follows.

Corollary. If the first 3 reference points $P_0(t_0, y_0)$, $P_1(t_1, y_1)$, and $P_2(t_2, y_2)$ are selected to satisfy $y_0 = y_1 = y_2$, then the developed Bézier curve $B(\alpha)$ will go across the first point and derivative of $B(\alpha)$ with respect to t at t_0 is zero. Similarly, if the last 3 points $P_{n-2}(t_{n-2}, y_{n-2})$, $P_{n-1}(t_{n-1}, y_{n-1})$, and $P_n(t_n, y_n)$ ($n \geq 3$) are selected to satisfy $y_{n-2} = y_{n-1} = y_n$, then $B(\alpha(T_a)) = y_n$ and $\text{d}B(\alpha)/\text{d}t = 0$.

Based on the aforementioned analysis, without loss of generality, a brand-new appointed-time convergent performance function $\mu(t)$ is generated by constructing a Bézier curve with 7 points. Namely, its detailed form is given by

$$\mu(t) = \begin{cases} \beta_0(\alpha)y_0 + \beta_1(\alpha)y_1 + \cdots + \beta_6(\alpha)y_6, \text{ if } t \leq T_a \\ y_6, \text{ if } t > T_a, \end{cases} \quad (17)$$

where $\beta_j(\alpha) = \frac{6!}{j!(6-j)!}\alpha^j(1-\alpha)^{6-j}$, $\alpha = t/T_a \in [0,1]$ $(j = 0, 1, \cdots, 6)$, $y_0 = y_1 = y_2 = \mu(0) = \mu_0$, and $y_4 = y_5 = y_6 = \mu(T_a) = \mu_\infty$ with $\mu_0 > \mu_\infty > 0$ being 2 constants. y_5 is selected to satisfy $y_5 \in (\mu_0, \mu_\infty)$ and can be adjusted for different convergent speed.

To verify the effectiveness of the proposed performance $\mu(t)$ in Eq. 17, a comparative simulation is carried out against the traditional appointed-time performance in [44] with the same initial value $\mu_0 = 8$, the same final value $\mu_\infty = 0.5$, and the same appointed time $T_a = 8$ s. The simulation result is presented in Fig. 2.

From Fig. 2, one can obtain that the initial convergent speed of the proposed function is obviously slower than the traditional one because of the initial zero derivative. In practical applications, the input saturation problem usually occurs at the initial time due to the big initial state errors. The proposed function provides a wider range for the tracking control system, by which the effect of the input saturation problem can be reduced. In the meantime, the appointed-time convergent property is remained.

Remark 1. Appointed-time convergent performance function proposed in Eq. 17 is defined by 7 reference points, with only $P_3(t_3, y_3)$ for adjusting the convergent speed. Actually, extra reference points can be inserted into the Bézier curve if the control system has complex requirements for the whole convergent process. Consequently, the proposed performance function $\mu(t)$ is more flexible than the traditional one in practical situations.

Anti-saturated appointed-time pose tracking controller design

In this part, an anti-saturated appointed-time pose tracking controller is designed to realize the performance function. Before moving, a vital assumption is given as follows.

Assumption. The uncertain accelerated velocity $\boldsymbol{a}_t$ of the tumbling target and space perturbations $\boldsymbol{d}$ and $\boldsymbol{\tau}_d$ in Eqs. 1 and 7 are bounded.

Remark 2. Owing to the physical limitations for the tumbling target, its accelerated velocity is bounded. Moreover, if the space perturbations are sufficiently large, the close-range proximity operations will not be completed with restricted control input. Thus, Assumption is reasonable.
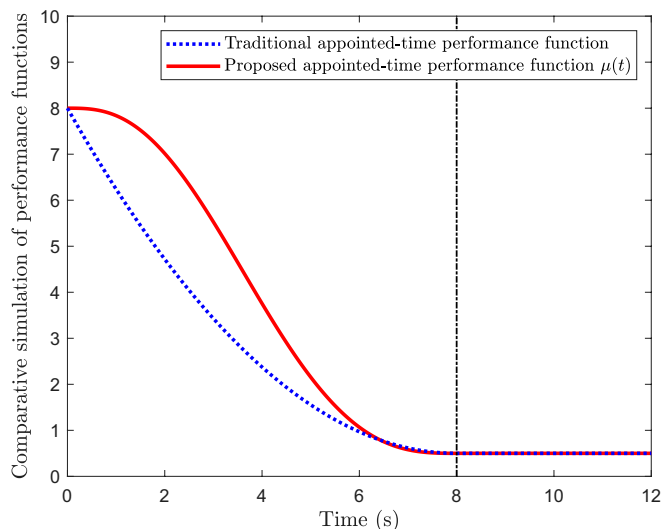

Fig. 2. Comparative simulation of different appointed-time performance functions.

To facilitate the subsequent controller design, an auxiliary state variable $\boldsymbol{p} \in \mathbb{R}^6$ is defined as

$$\boldsymbol{p} = \boldsymbol{\chi}_2 + \lambda\boldsymbol{\phi}(\boldsymbol{\chi}_1), \tag{18}$$

where $\lambda = \operatorname{diag}\{\lambda_1, \lambda_2, ..., \lambda_6\} \in \mathbb{R}^{6\times6}$ is positive-definite diagonal matrix. Based on [41], the element of vector $\boldsymbol{\phi}(\boldsymbol{\chi}_1)$ is designed in the following form

$$\phi(\chi_{1,i}) = \begin{cases} \operatorname{sgn}^\gamma(\chi_{1,i}), \text{if } |\chi_{1,i}| > \varepsilon_{0,i}, p_i \neq 0 \text{ or } p_i = 0 \\ b_{1,i}\chi_{1,i} + b_{2,i}\operatorname{sgn}^2(\chi_{1,i}), \text{if } |\chi_{1,i}| \leq \varepsilon_{0,i} \ \& \ p_i \neq 0, \end{cases} \tag{19}$$

where $\gamma \in (0,1)$, $0 < \varepsilon_{0,i} \leq \left(\frac{\mu_{i,\infty}}{\lambda_i}\right)^{\frac{1}{\gamma}}$, $b_{1,i} = (2-\gamma)\varepsilon_{0,i}^{\gamma-1}$, and $b_{2,i} = (\gamma-1)\varepsilon_{0,i}^{\gamma-2}$ are design parameters. $\operatorname{sgn}^\gamma(\chi_{1,i}) = |\chi_{1,i}|^\gamma \operatorname{sgn}(\chi_{1,i})$. $\operatorname{sgn}^2(\chi_{1,i}) = |\chi_{1,i}|^2 \operatorname{sgn}(\chi_{1,i})$. Then, the time derivative of $\phi(\chi_{1,i})$ in Eq. 19 equals to

$$\dot{\phi}(\chi_{1,i}) = \begin{cases} \gamma|\chi_{1,i}|^{\gamma-1}\dot{\chi}_{1,i}, \text{if } |\chi_{1,i}| > \varepsilon_{0,i}, p_i \neq 0 \text{ or } p_i = 0 \\ b_{1,i}\dot{\chi}_{1,i} + 2b_{2,i}|\chi_{1,i}|\dot{\chi}_{1,i}, \text{if } |\chi_{1,i}| \leq \varepsilon_{0,i} \ \& \ p_i \neq 0. \end{cases} \tag{20}$$

To guarantee the pose tracking performance during the close-range proximity operations, the following performance inequality is imposed on the auxiliary state variable $\boldsymbol{p} = [p_1, p_2, ..., p_6]^{\mathsf{T}}$ as

$$\begin{cases} -\delta_i\mu_i(t) < p_i(t) < \mu_i(t) & \text{if } p_i(0) \geq 0 \\ -\mu_i(t) < p_i(t) < \delta_i\mu_i(t) & \text{if } p_i(0) < 0, \end{cases} \tag{21}$$

where $\mu_i(t)$ $(i = 1, 2, ..., 6)$ is derived from Eq. 17. $\delta_i \in (0,1]$ is a positive constant. Then, the standard tracking error $\Lambda_i = p_i(t)/\mu_i(t)$ satisfies

$$\Lambda_i = \frac{p_i(t)}{\mu_i(t)} \in \Omega_i = (-\underline{\delta}_i, \overline{\delta}_i) = \begin{cases} (-\delta_i, 1), \text{if } p_i(0) \geq 0 \\ (-1, \delta_i), \text{if } p_i(0) < 0. \end{cases} \tag{22}$$

In PPC structure, a constraint-free translation function is often used to remove the defined performance constraints as presented in Eq. 21. Namely, there exists a monotone function $\mathcal{P}(\bullet)$ such that

$$\begin{cases} p_i(t) = \mathcal{P}(\theta_i)\mu_i(t) \\ \lim_{\theta_i \to +\infty} \mathcal{P}(\theta_i) = \overline{\delta}_i \\ \lim_{\theta_i \to -\infty} \mathcal{P}(\theta_i) = -\underline{\delta}_i, \end{cases} \tag{23}$$

where $\theta_i \in \mathbb{R}$ is the newly established state variable. Without loss of generality, function $\mathcal{P}(\bullet)$ in this work is chosen as $\mathcal{P}(\theta_i) = [\overline{\delta}_i\underline{\delta}_i(\exp(2\theta_i) - 1)]/[\underline{\delta}_i\exp(2\theta_i) + \overline{\delta}_i]$. Then, the newly established state is obtained as

$$\theta_i = \mathcal{P}^{-1}(\Lambda_i) = \frac{1}{2}\ln\left(\frac{\overline{\delta}_i\underline{\delta}_i + \overline{\delta}_i\Lambda_i}{\overline{\delta}_i\underline{\delta}_i - \underline{\delta}_i\Lambda_i}\right). \tag{24}$$

Based on the foregoing analysis, an adaptive anti-saturated appointed-time pose tracking controller is devised for system Eq. 14 as

$$\boldsymbol{u} = \underbrace{\boldsymbol{u}_0}_{\text{stable control term}} + \underbrace{\boldsymbol{u}_c}_{\text{anti-saturation control term}},$$

(25)

with

$$\boldsymbol{u}_0 = -\boldsymbol{k}\boldsymbol{\xi}\boldsymbol{\theta} - \lambda\dot{\boldsymbol{\phi}}(\boldsymbol{\chi}_1) + \text{diag}\left\{\frac{\dot{\boldsymbol{\mu}}(t)}{\boldsymbol{\mu}(t)}\right\}\boldsymbol{p} - \frac{\widehat{\varpi}\psi^2(\boldsymbol{x})\boldsymbol{\Lambda}}{\psi(\boldsymbol{x})\|\boldsymbol{\Lambda}\| + \iota_0},$$

(26)

$\boldsymbol{u}_c$ is derived by the following adaptive projection rule

$$\dot{\boldsymbol{u}}_c = \text{Proj}(\boldsymbol{u}_c, \boldsymbol{\Lambda}) = \begin{cases} -\kappa_1\boldsymbol{u}_c - \dfrac{\boldsymbol{u}_c\boldsymbol{\Lambda}^\top\text{diag}^{-1}\{\boldsymbol{\mu}(t)\}(\boldsymbol{u}_c + \Delta\boldsymbol{u})}{\boldsymbol{u}_c^\top\boldsymbol{u}_c + |\rho_0|}, & \text{if}\|\boldsymbol{u}_c\| \geq \Xi_0 \\ 0, & \text{otherwise}, \end{cases}$$

$$\dot{\rho}_0 = \text{Proj}(\rho_0, \boldsymbol{\Lambda}) = \begin{cases} -\kappa_2\rho_0 - \dfrac{\text{sign}(\rho_0)\boldsymbol{\Lambda}^\top\text{diag}^{-1}\{\boldsymbol{\mu}(t)\}(\boldsymbol{u}_c + \Delta\boldsymbol{u})}{\boldsymbol{u}_c^\top\boldsymbol{u}_c + |\rho_0|}, & \text{if}\|\boldsymbol{u}_c\| \geq \Xi_0 \\ 0, & \text{otherwise}, \end{cases}$$

(27)

where $\boldsymbol{k} = \text{diag}\{k_1, k_2, \ldots, k_6\}$ and $\boldsymbol{\xi} = \text{diag}\{\xi_1, \xi_2, \ldots, \xi_6\} \in \mathbb{R}^{6\times6}$ are, respectively, the positive-definite control gain matrix and intermediate parameters. Wherein, each element of $\boldsymbol{\xi}$ equals to $\xi_i = \overline{\delta}_i\underline{\delta}_i / \left[(\Lambda_i + \underline{\delta}_i)(\overline{\delta}_i - \Lambda_i)(\overline{\delta}_i + \underline{\delta}_i)\right]$ $(i = 1, 2, \ldots, 6)$. $\Delta\boldsymbol{u} = \text{sat}(\boldsymbol{u}) - \boldsymbol{u}$ is the difference between control input command and the output of the actuator. ι_0 and Ξ_0 are 2 small positive constants. κ_1 and κ_2 are the relevant positive constants. $\psi(\boldsymbol{x})$ is the product of the 2-norm of the Gaussian basis function $\boldsymbol{\varphi}(\boldsymbol{x})$, i.e, $\psi(\boldsymbol{x}) = \|\boldsymbol{\varphi}(\boldsymbol{x})\|$. $\widehat{\varpi}$ is an adaptive parameter to be defined later, which has the following adaptive law

$$\dot{\widehat{\varpi}} = -\kappa_3\widehat{\varpi} + \frac{\psi^2(\boldsymbol{x})\boldsymbol{\Lambda}^\top\boldsymbol{\Lambda}}{\psi(\boldsymbol{x})\|\boldsymbol{\Lambda}\| + \iota_0},$$

(28)

where κ_3 is a positive constant.

Remark 3. Based on the devised performance function in Eq. 17, it is easy to find that the zero derivative of the performance function makes the tracking error system response more smooth. This is conducive to reduce the existence of saturation phenomenon. Moreover, the anti-saturated pose tracking controller devised in Eq. 27 is also used to compensate the negative effects induced by the actuator saturation. Thus, there are 2 anti-saturation ways in our work.

Stability analysis

Based on the aforementioned anti-saturated appointed-time pose tracking controller design, an important result is addressed in the following theorem.

Theorem. Under the devised pose controller and adaptive laws in Eqs. 24 to 28, when the control gain k_i satisfies $k_i > (1 + \delta_i)^2/8$ $(i = 1, 2, \ldots, 6)$, the auxiliary state variable $\boldsymbol{p}$ will be steered to a small neighborhood around origin with guaranteed prescribed performance within appointed time instant $T_{a,\max} = \max\{T_{a,i}\}$ $(i = 1, 2, \ldots, 6)$. Both the pose tracking errors $\boldsymbol{\chi}_1$ and $\boldsymbol{\chi}_2$ are finite-time convergent. Moreover, all the involved close-loop signals for the close-range proximity operations are uniformly ultimately bounded.

Proof. The proof of Theorem is divided into 2 steps as follows.

Step 1. Prove the convergence of the auxiliary tracking error $\boldsymbol{p}$ for close-range proximity operations within appointed time

instant $T_{a,\max} = \max\{T_{a,i}\}$ $(i = 1, 2, \ldots, 6)$. First, considering $\Lambda_i = p_i/\mu_i(t)$ $(i = 1, 2, \ldots, 6)$, there exists

$$\dot{\Lambda}_i = \left(\frac{p_i}{\mu_i(t)}\right)' = \frac{\dot{p}_i}{\mu_i(t)} - \frac{\dot{\mu}_i(t)}{\mu_i^2(t)}p_i.$$

(29)

The above equation is also equivalent to $\dot{\boldsymbol{\Lambda}} = \text{diag}^{-1}\{\boldsymbol{\mu}(t)\}\left[\dot{\boldsymbol{p}} - \text{diag}\{\dot{\boldsymbol{\mu}}(t)/\boldsymbol{\mu}(t)\}\boldsymbol{p}\right]$ To guarantee the prescribed pose tracking performance in the close-range operations defined in Eq. 21, the following Lyapunov function V_1 is constructed

$$\begin{cases} V_1 = V_{11} + V_{12} \\ V_{11} = \dfrac{1}{2}\boldsymbol{\Lambda}^\top\boldsymbol{\Lambda} \\ V_{12} = \dfrac{1}{2}\boldsymbol{u}_c^\top\boldsymbol{u}_c + \dfrac{1}{2}\rho_0^2 + \dfrac{\mu_{\min}}{2}\widetilde{\varpi}^2, \end{cases}$$

(30)

where $\mu_{\min} = \min\limits_{i=1,2,\ldots,6}\{1/\mu_{i,0}\}$. $\widetilde{\varpi} = \varpi - \widehat{\varpi}$ is the estimation error. Based on Eq. 30, taking the time derivative of V_1 yields

$$\begin{aligned} \dot{V}_{11} &= \boldsymbol{\Lambda}^\top\dot{\boldsymbol{\Lambda}} \\ &= \boldsymbol{\Lambda}^\top\text{diag}^{-1}\{\boldsymbol{\mu}(t)\}\left[\dot{\boldsymbol{p}} - \text{diag}^{-1}\{\boldsymbol{\mu}(t)\}\text{diag}\{\dot{\boldsymbol{\mu}}(t)\}\boldsymbol{p}\right]. \end{aligned}$$

(31)

Substituting Eqs. 14, 20, and 25 into Eq. 31 gets

$$\dot{V}_{11} = \boldsymbol{\Lambda}^\top\text{diag}^{-1}\{\boldsymbol{\mu}(t)\}\left[\boldsymbol{f}_1^*(\boldsymbol{\chi}_1, \boldsymbol{\chi}_2) + \text{sat}(\boldsymbol{u}) + \lambda\dot{\boldsymbol{\phi}}(\boldsymbol{\chi}_1) - \text{diag}^{-1}\{\boldsymbol{\mu}(t)\}\text{diag}\{\dot{\boldsymbol{\mu}}(t)\}\boldsymbol{p}\right]$$

$$= \boldsymbol{\Lambda}^\top\text{diag}^{-1}\{\boldsymbol{\mu}(t)\}\left[\boldsymbol{f}_1^*(\boldsymbol{\chi}_1, \boldsymbol{\chi}_2) + \boldsymbol{u} + \Delta\boldsymbol{u} + \lambda\dot{\boldsymbol{\phi}}(\boldsymbol{\chi}_1) - \text{diag}^{-1}\{\boldsymbol{\mu}(t)\}\text{diag}\{\dot{\boldsymbol{\mu}}(t)\}\boldsymbol{p}\right]$$

$$= \boldsymbol{\Lambda}^\top\text{diag}^{-1}\{\boldsymbol{\mu}(t)\}\left[-\boldsymbol{k}\boldsymbol{\xi}\boldsymbol{\theta} - \frac{\widehat{\varpi}\psi^2(\boldsymbol{x})\boldsymbol{\Lambda}}{\psi(\boldsymbol{x})\|\boldsymbol{\Lambda}\| + \iota_0} + \boldsymbol{u}_c + \Delta\boldsymbol{u} + \boldsymbol{f}_1^*(\boldsymbol{\chi}_1, \boldsymbol{\chi}_2)\right]$$

$$\leq -\sum_{i=1}^{6}\frac{k_i\Lambda_i\xi_i\theta_i}{\mu_i(t)} - \mu_{\min}\frac{\widehat{\varpi}\psi^2(\boldsymbol{x})\boldsymbol{\Lambda}^\top\boldsymbol{\Lambda}}{\psi(\boldsymbol{x})\|\boldsymbol{\Lambda}\| + \iota_0} + \boldsymbol{\Lambda}^\top\text{diag}^{-1}\{\boldsymbol{\mu}(t)\}\left[\boldsymbol{f}_1^*(\boldsymbol{\chi}_1, \boldsymbol{\chi}_2) + \boldsymbol{u}_c + \Delta\boldsymbol{u}\right]$$

(32)

To facilitate the subsequent simplification for Eq. 32, we define a function as follows

$$\hbar(\Lambda_i) = \frac{1}{\Lambda_i}\ln\left(\frac{\overline{\delta}_i\underline{\delta}_i + \overline{\delta}_i\Lambda_i}{\overline{\delta}_i\underline{\delta}_i - \underline{\delta}_i\Lambda_i}\right) \quad (i = 1, 2, \ldots, 6),$$

(33)

Taking the derivative of $\hbar(\Lambda_i)$ with respect to Λ_i gets

$$\dot{\hbar}(\Lambda_i) = \frac{\mathrm{d}\hbar}{\mathrm{d}\Lambda_i} = \frac{1}{\Lambda_i}\left[\frac{\overline{\delta}_i + \underline{\delta}_i}{(\Lambda_i + \underline{\delta}_i)(\overline{\delta}_i - \Lambda_i)} - \frac{1}{\Lambda_i}\ln\left(\frac{\overline{\delta}_i\underline{\delta}_i + \overline{\delta}_i\Lambda_i}{\overline{\delta}_i\underline{\delta}_i - \underline{\delta}_i\Lambda_i}\right)\right]$$

(34)

As the above equation presents, it is easy to verify that when $0 < \Lambda_i < \overline{\delta}_i, \hbar(\Lambda_i) > 0$ and when $-\underline{\delta}_i < \Lambda_i < 0, \hbar(\Lambda_i) < 0$. Thus, one can obtain the minimal value $\hbar_{\min}$ of function $\hbar(\Lambda_i)$, namely, it is derived by applying the L'Hospital's rule

$$\begin{aligned} \hbar_{\min}(\Lambda_i) &= \lim_{\Lambda_i\to0^+}\hbar_{\min}(\Lambda_i) = \lim_{\Lambda_i\to0^-}\hbar_{\min}(\Lambda_i) \\ &= \frac{\mathrm{d}2\theta_i/\mathrm{d}\Lambda_i}{1}\bigg|_{\Lambda_i=0} = \frac{\overline{\delta}_i + \underline{\delta}_i}{(\Lambda_i + \underline{\delta}_i)(\overline{\delta}_i - \Lambda_i)}\bigg|_{\Lambda_i=0} \\ &= \frac{\overline{\delta}_i + \underline{\delta}_i}{\overline{\delta}_i\underline{\delta}_i} \end{aligned}$$

(35)

Based on the above equation, the following inequality holds

$$\Lambda_i \xi_i \theta_i = \frac{\Lambda_i \overline{\delta}_i \underline{\delta}_i}{(\Lambda_i + \underline{\delta}_i)(\overline{\delta}_i - \Lambda_i)(\overline{\delta}_i + \underline{\delta}_i)} \times \ln\left(\frac{\overline{\delta}_i \underline{\delta}_i + \overline{\delta}_i \Lambda_i}{\overline{\delta}_i \underline{\delta}_i - \underline{\delta}_i \Lambda_i}\right) \leq \frac{\Lambda_i^2}{(\Lambda_i + \underline{\delta}_i)(\overline{\delta}_i - \Lambda_i)}.$$
(36)

According to Eq. 14, one can find that term $\boldsymbol{\Lambda}^\top \mathrm{diag}^{-1}\{\boldsymbol{\mu}(t)\}\boldsymbol{f}_1^*(\boldsymbol{\chi}_1, \boldsymbol{\chi}_2)$ satisfies

$$\begin{aligned}
\|\boldsymbol{\Lambda}^\top \mathrm{diag}^{-1}\{\boldsymbol{\mu}(t)\}\boldsymbol{f}_1^*(\boldsymbol{\chi}_1, \boldsymbol{\chi}_2)\| &\leq \|\mathrm{diag}^{-1}\{\boldsymbol{\mu}(t)\}\|\|\boldsymbol{\Lambda}\|\|\boldsymbol{f}_1^*(\boldsymbol{\chi}_1, \boldsymbol{\chi}_2)\| \\
&\leq \mu_{\min}\frac{\mu_{\max}}{\mu_{\min}}\|\mathcal{W}\|\|\boldsymbol{\Lambda}\|\|\boldsymbol{\varphi}(\boldsymbol{x})\| \\
&\leq \mu_{\min}\varpi\|\boldsymbol{\Lambda}\|\psi(\boldsymbol{x}),
\end{aligned}$$
(37)

where $\mu_{\max} = \max_{i=1,2,\ldots,6}\{1/\mu_{i,\infty}\}$. $\varpi = \mu_{\max}\|\mathcal{W}\|/\mu_{\min}$. $\psi(\boldsymbol{x})$ is defined in Eq. 27. Based on Eqs. 36 and 37, Eq. 32 becomes

$$\begin{aligned}
\dot{V}_{11} \leq &-\sum_{i=1}^{6}\frac{k_i\Lambda_i^2}{\mu_i(t)(\Lambda_i + \underline{\delta}_i)(\overline{\delta}_i - \Lambda_i)} + \boldsymbol{\Lambda}^\top\mathrm{diag}^{-1}\{\boldsymbol{\mu}(t)\}(\boldsymbol{u}_c + \Delta\boldsymbol{u}) \\
&+ \mu_{\min}\left(\varpi\|\boldsymbol{\Lambda}\|\psi(\boldsymbol{x}) - \frac{\hat{\varpi}\psi^2(\boldsymbol{x})\boldsymbol{\Lambda}^\top\boldsymbol{\Lambda}}{\psi(\boldsymbol{x})\|\boldsymbol{\Lambda}\| + \iota_0}\right) \\
\leq &-\sum_{i=1}^{6}\frac{k_i\Lambda_i^2}{\mu_i(t)(\Lambda_i + \underline{\delta}_i)(\overline{\delta}_i - \Lambda_i)} + \boldsymbol{\Lambda}^\top\mathrm{diag}^{-1}\{\boldsymbol{\mu}(t)\}(\boldsymbol{u}_c + \Delta\boldsymbol{u}) \\
&+ \mu_{\min}\left(\frac{\tilde{\varpi}\psi^2(\boldsymbol{x})\boldsymbol{\Lambda}^\top\boldsymbol{\Lambda}}{\psi(\boldsymbol{x})\|\boldsymbol{\Lambda}\| + \iota_0} + \frac{\varpi\|\boldsymbol{\Lambda}\|\psi(\boldsymbol{x})\iota_0}{\psi(\boldsymbol{x})\|\boldsymbol{\Lambda}\| + \iota_0}\right) \\
\leq &-\sum_{i=1}^{6}\frac{k_i\Lambda_i^2}{\mu_i(t)(\Lambda_i + \underline{\delta}_i)(\overline{\delta}_i - \Lambda_i)} + \boldsymbol{\Lambda}^\top\mathrm{diag}^{-1}\{\boldsymbol{\mu}(t)\}(\boldsymbol{u}_c + \Delta\boldsymbol{u}) \\
&+ \mu_{\min}\left(\frac{\tilde{\varpi}\psi^2(\boldsymbol{x})\boldsymbol{\Lambda}^\top\boldsymbol{\Lambda}}{\psi(\boldsymbol{x})\|\boldsymbol{\Lambda}\| + \iota_0} + \iota_0\varpi\right)
\end{aligned}$$
(38)

With consideration of $\tilde{\varpi} = \varpi - \hat{\varpi}$, $\dot{\tilde{\varpi}} = \dot{\varpi} - \dot{\hat{\varpi}} = -\dot{\hat{\varpi}}$, then, taking the derivative of V_{12} in Eq. 30 yields

$$\dot{V}_{12} = \boldsymbol{u}_c^\top\dot{\boldsymbol{u}}_c + \rho_0\dot{\rho}_0 + \mu_{\min}\tilde{\varpi}\dot{\tilde{\varpi}}.$$
(39)

Accordingly, 2 cases are considered as follows.

Case 1.1: $\|\boldsymbol{u}_c\| \geq \Xi_0$. Then, substituting the first 2 subequations in Eq. 27 into Eq. 39 gets

$$\begin{aligned}
\dot{V}_{12} = &-\kappa_1\boldsymbol{u}_c^\top\boldsymbol{u}_c - \frac{\boldsymbol{u}_c^\top\boldsymbol{u}_c\boldsymbol{\Lambda}^\top\mathrm{diag}^{-1}\{\boldsymbol{\mu}(t)\}(\boldsymbol{u}_c + \Delta\boldsymbol{u})}{\boldsymbol{u}_c^\top\boldsymbol{u}_c + |\rho_0|} \\
&-\kappa_2\rho_0^2 - \frac{|\rho_0|\boldsymbol{\Lambda}^\top\mathrm{diag}^{-1}\{\boldsymbol{\mu}(t)\}(\boldsymbol{u}_c + \Delta\boldsymbol{u})}{\boldsymbol{u}_c^\top\boldsymbol{u}_c + |\rho_0|} - \mu_{\min}\tilde{\varpi}\dot{\hat{\varpi}} \\
= &-\kappa_1\boldsymbol{u}_c^\top\boldsymbol{u}_c - \kappa_2\rho_0^2 - \mu_{\min}\tilde{\varpi}\dot{\hat{\varpi}} - \boldsymbol{\Lambda}^\top\mathrm{diag}^{-1}\{\boldsymbol{\mu}(t)\}(\boldsymbol{u}_c + \Delta\boldsymbol{u}).
\end{aligned}$$
(40)

Based on Eqs. 28, 38, and 40, the derivative of V_1 in Eq. 30 satisfies

$$\begin{aligned}
\dot{V}_1 = \dot{V}_{11} + \dot{V}_{12} \leq &-\sum_{i=1}^{6}\frac{k_i\Lambda_i^2}{\mu_i(t)(\Lambda_i + \underline{\delta}_i)(\overline{\delta}_i - \Lambda_i)} - \kappa_1\boldsymbol{u}_c^\top\boldsymbol{u}_c - \kappa_2\rho_0^2 \\
&+ \mu_{\min}\tilde{\varpi}\left(\frac{\psi^2(\boldsymbol{x})\boldsymbol{\Lambda}^\top\boldsymbol{\Lambda}}{\psi(\boldsymbol{x})\|\boldsymbol{\Lambda}\| + \iota_0} - \dot{\hat{\varpi}}\right) + \varpi\iota_0\mu_{\min} \\
\leq &-\sum_{i=1}^{6}\frac{k_i\Lambda_i^2}{\mu_i(t)(\Lambda_i + \underline{\delta}_i)(\overline{\delta}_i - \Lambda_i)} - \kappa_1\boldsymbol{u}_c^\top\boldsymbol{u}_c - \kappa_2\rho_0^2 \\
&- \frac{\mu_{\min}\kappa_3}{2}\tilde{\varpi}^2 + \frac{\mu_{\min}\kappa_3}{2}\varpi^2 + \varpi\iota_0\mu_{\min} \\
\leq &-\sum_{i=1}^{6}\frac{k_i\Lambda_i^2}{\mu_i(t)(\Lambda_i + \underline{\delta}_i)(\overline{\delta}_i - \Lambda_i)} - \kappa_1\boldsymbol{u}_c^\top\boldsymbol{u}_c - \kappa_2\rho_0^2 - \frac{\mu_{\min}\kappa_3}{2}\tilde{\varpi}^2 + \aleph_0
\end{aligned}$$
(41)

where $\aleph_0 = \mu_{\min}\kappa_3\varpi^2/2 + \varpi\iota_0\mu_{\min}$ is a positive constant.

Accordingly, there exists $\mathcal{E}_0 = \min_{i=1,2,\ldots,6}\{2k_i/[\mu_{i,0}(\Lambda_{i,\max} + \underline{\delta}_i)(\overline{\delta}_i - \Lambda_{i,\min})], 2\kappa_1, 2\kappa_2, \mu_{\min}\kappa_3\}$ such that

$$\dot{V}_1 \leq -\mathcal{E}_0 V_1 + \aleph_0,$$
(42)

Based on Eq. 42, one can obtain that $V_1 \leq \exp(-\mathcal{E}_0 t)\left(V_1(0) - \frac{\aleph_0}{\mathcal{E}_0}\right) + \frac{\aleph_0}{\mathcal{E}_0}$. Thus, when $\|\boldsymbol{u}_c\| \geq \Xi_0$, all the adaptive parameters are uniformly ultimately bounded. Meanwhile, owing to the appointed-time convergence of the performance function $\mu_i(t)$, one can find that the state variable p_i is appointed-time convergent to the envelope generated by the steady-state performance bound $\mu_{i,\infty}$ ($i = 1, 2, \ldots, 6$).

Case 1.2: $\|\boldsymbol{u}_c\| < \Xi_0$. Then, substituting the second 2 subequations in Eq. 27 into Eq. 39 gets

$$\dot{V}_{12} = -\mu_{\min}\tilde{\varpi}\dot{\hat{\varpi}}$$
(43)

In this regard, based on Eqs. 28, 38, and 43, the derivative of V_1 in Eq. 30 satisfies

$$\begin{aligned}
\dot{V}_1 = \dot{V}_{11} + \dot{V}_{12} \leq &-\sum_{i=1}^{6}\frac{k_i\Lambda_i^2}{\mu_i(t)(\Lambda_i + \underline{\delta}_i)(\overline{\delta}_i - \Lambda_i)} + \boldsymbol{\Lambda}^\top\mathrm{diag}^{-1}\{\boldsymbol{\mu}(t)\}\times \\
&(\boldsymbol{u}_c + \Delta\boldsymbol{u}) + \mu_{\min}\tilde{\varpi}\left(\frac{\psi^2(\boldsymbol{x})\boldsymbol{\Lambda}^\top\boldsymbol{\Lambda}}{\psi(\boldsymbol{x})\|\boldsymbol{\Lambda}\| + \iota_0} - \dot{\hat{\varpi}}\right) + \varpi\iota_0\mu_{\min} \\
\leq &-\sum_{i=1}^{6}\frac{\Lambda_i^2}{\mu_i(t)}\left(\frac{k_i}{(\Lambda_i + \underline{\delta}_i)(\overline{\delta}_i - \Lambda_i)} - \frac{1}{2}\right) - \frac{\mu_{\min}\kappa_3}{2}\tilde{\varpi}^2 \\
&+ \frac{\mu_{\min}\kappa_3}{2}\varpi^2 + \varpi\iota_0\mu_{\min} + \frac{1}{2}\sum_{i=1}^{6}\frac{(u_{c,i} + \Delta u_i)^2}{\mu_i(t)}
\end{aligned}$$

$$\leq -\sum_{i=1}^{6} \frac{\Lambda_i^2}{\mu_i(t)}\left(\frac{k_i}{(\Lambda_i+\underline{\delta}_i)(\overline{\delta}_i-\Lambda_i)}-\frac{1}{2}\right)-\frac{\mu_{\min}\kappa_3}{2}\tilde{\varpi}^2+\aleph_0$$

(44)

where $\aleph_0=\mu_{\min}\kappa_3\varpi^2/2+\varpi\iota_0\mu_{\min}+\max\left\{\frac{1}{2}\sum_{i=1}^{6}\left(u_{c,i}+\Delta u_i\right)^2/\mu_i(t)\right\}$ is a lumped term. Note that Ξ_0 is very small positive constant. In this case, the anti-saturation controller term $\boldsymbol{u}_c$ is very small, which in turn means that the difference $\Delta\boldsymbol{u}$ between the desired control input command $\boldsymbol{u}$ and actuator output $\text{sat}(\boldsymbol{u})$ is very small. Thus, term $\frac{1}{2}\sum_{i=1}^{6}\left(u_{c,i}+\Delta u_i\right)^2/\mu_i(t)$ is bounded by a small constant, and the lumped term $\aleph_0$ is bounded. For term $\frac{k_i}{(\Lambda_i+\underline{\delta}_i)(\overline{\delta}_i-\Lambda_i)}-\frac{1}{2}$, when it is large than zero, one can find that $k_1>\frac{1}{2}(\Lambda_i+\underline{\delta}_i)(\overline{\delta}_i-\Lambda_i)$. Considering Λ_i, $\overline{\delta}_i$, and $\underline{\delta}_i$ defined in Eq. 22, it is easy to obtain that the maximal value of function $\frac{1}{2}(\Lambda_i+\underline{\delta}_i)(\overline{\delta}_i-\Lambda_i)$ with respect to the variable Λ_i, namely, its maximal value is $(1+\delta_i)^2/8$ $(i=1,2,\ldots,6)$. Thus, when $k_i>(1+\delta_i)^2/8$ $(i=1,2,\ldots,6)$, the following stability analysis is similar to that as presented in Case 1.1, which is omitted for brevity.

Consequently, based on the stability analysis in Case 1.1 and Case 1.2, one can find that, when $k_i>(1+\delta_i)^2/8$ $(i=1,2,\ldots,6)$, the defined auxiliary state variable $\boldsymbol{p}$ is appointed-time convergent to the steady-state performance bound within time instant $T_{a,\max}=\max\{T_{a,i}(i=1,2,\ldots,6)\}$ and all the adaptive parameters are uniformly ultimately bounded.

Step 2. The finite-time convergence analysis for the pose tracking errors χ_1 and χ_2.

Case 2.1: When $p_i=0$ $(i=1,2,\ldots,6)$, based on Eq. 18, one can obtain that

$$\chi_{2,i}+\lambda_i\phi(\chi_{1,i})=0.$$

(45)

Then, the following Lyapunov function is defined

$$V_{2,i}=\frac{1}{2}\chi_{1,i}^2.$$

(46)

Substituting Eq. 45 into the time derivative of $V_{2,i}$ yields

$$\begin{aligned}\dot{V}_{2,i}&=\chi_{1,i}\dot{\chi}_{1,i}=\chi_{1,i}\chi_{2,i}\\&=-\lambda_i\chi_{1,i}\phi(\chi_{1,i})\\&=-\lambda_i\chi_{1,i}\text{sgn}^\gamma(\chi_{1,i})\\&=-\lambda_i\chi_{1,i}|\chi_{1,i}|^\gamma\text{sgn}(\chi_{1,i})\\&=-\lambda_i|\chi_{1,i}|^{\gamma+1}=-\lambda_i2^{\frac{\gamma+1}{2}}V_{2,i}^{\frac{\gamma+1}{2}}.\end{aligned}$$

(47)

According to Theorem 4.2 in [45], one can find that the tracking error $\chi_{1,i}$ will converge to zero when $t\geq T_{a,\max}+T_{1,i}$ with $T_{1,i}$ satisfying

$$T_{1,i}\leq\frac{1}{\lambda_i2^{\frac{\gamma+1}{2}}\left(1-\frac{\gamma+1}{2}\right)}V_{2,i}^{1-\frac{\gamma+1}{2}}(\chi_{1,i}(0))=\frac{2^{\frac{1-\gamma}{2}}}{\lambda_i(1-\gamma)}V_{2,i}^{\frac{1-\gamma}{2}}(\chi_{1,i}(0))$$

(48)

Case 2.2: When $p_i\in\left(-\underline{\delta}_i\mu_{i,\infty},0\right)\cup\left(0,\overline{\delta}_i\mu_{i,\infty}\right)|\chi_{1,i}|\geq\varepsilon_{0,i}$ $(i=1,2,\ldots,6)$, based on Eq. 18, one can obtain that

$$\chi_{2,i}+\lambda_i\phi(\chi_{1,i})=p_i\in\left(\underline{\delta}_i\mu_{i,\infty},\overline{\delta}_i\mu_{i,\infty}\right).$$

(49)

Equation 49 is equivalent to

$$\begin{aligned}\dot{\chi}_{1,i}&=-\left(\lambda_i-\frac{p_i}{\text{sgn}^\gamma(\chi_{1,i})}\right)\text{sgn}^\gamma(\chi_{1,i})\\&=-\left(\lambda_i-\frac{p_i}{|\chi_{1,i}|^\gamma\text{sgn}(\chi_{1,i})}\right)|\chi_{1,i}|^\gamma\text{sgn}(\chi_{1,i}).\end{aligned}$$

(50)

Based on the above equation, when $\lambda_i-\frac{p_i}{|\chi_{1,i}|^\gamma\text{sgn}(\chi_{1,i})}\leq0$, tracking error $\chi_{1,i}$ is convergent. If the Lyapunov function is chosen in the same form with Eq. 46, substituting Eq. 50 into the time derivative of $V_{2,i}$ can yield the similar form in Eq. 47. Thus, tracking error $\chi_{1,i}$ is finite-time convergent within $(T_{a,\max}+T_{2,i})$, wherein the detailed form of $T_{2,i}$ is similar to $T_{1,i}$ as presented in Eq. 48. The convergence domain of $\chi_{1,i}$ is expressed by

$$\lambda_i-\frac{p_i}{|\chi_{1,i}|^\gamma\text{sgn}(\chi_{1,i})}\leq0\Rightarrow|\chi_{1,i}|^\gamma\leq\frac{p_i}{\lambda_i}\Rightarrow\chi_{1,i}\leq\left(\frac{p_i}{\lambda_i}\right)^{1/\gamma}\leq\left(\frac{\mu_{i,\infty}}{\lambda_i}\right)^{1/\gamma}.$$

(51)

Case 2.3: When $p_i\in\left(-\underline{\delta}_i\mu_{i,\infty},0\right)\cup\left(0,\overline{\delta}_i\mu_{i,\infty}\right)|\chi_{1,i}|<\varepsilon_{0,i}=\left(\frac{\mu_{i,\infty}}{\lambda_i}\right)^{1/\gamma}$. According to the analysis in Case 2.2, one can find that when $|\chi_{1,i}|<\varepsilon_{0,i}=\left(\frac{\mu_{i,\infty}}{\lambda_i}\right)^{1/\gamma}$, $\chi_{1,i}$ is finite-time convergent within $(T_{a,\max}+T_{2,i})$. Thus, based on Eqs. 18 and 19, one can obtain that

$$\begin{aligned}|\chi_{2,i}|&=|p_i-\lambda_i\phi(\chi_{1,i})|\\&\leq|p_i|+\lambda_i|\phi(\chi_{1,i})|\\&=|p_i|+\lambda_i|b_{1,i}\chi_{1,i}+b_{2,i}\text{sgn}^2(\chi_{1,i})|\\&\leq|p_i|+\lambda_i|b_{1,i}\chi_{1,i}|+\lambda_i|b_{2,i}\text{sgn}^2(\chi_{1,i})|\\&\leq|p_i|+\lambda_i\left(b_{1,i}|\chi_{1,i}|+b_{2,i}|\chi_{1,i}|^2\right)\\&<|p_i|+\lambda_i\left(b_{1,i}\varepsilon_{0,i}+b_{2,i}\varepsilon_{0,i}^2\right)\\&=|p_i|+\lambda_i\left[(2-\gamma)\varepsilon_{0,i}^{\gamma-1}\varepsilon_{0,i}+(\gamma-1)\varepsilon_{0,i}^{\gamma-2}\varepsilon_{0,i}^2\right]\\&=|p_i|+\lambda_i\left[(2-\gamma)\varepsilon_{0,i}^\gamma+(\gamma-1)\varepsilon_{0,i}^\gamma\right]\\&=|p_i|+\lambda_i\varepsilon_{0,i}^\gamma\\&=|p_i|+\mu_{i,\infty}\\&\leq2\mu_{i,\infty}\end{aligned}$$

(52)

Accordingly to the stability analysis in Step 1 and Step 2 above, the proof of Theorem is completed.

Results

In this section, 2 simulation examples of close-range proximity control with a tumbling non-cooperative target are organized to verify the effectiveness of the proposed adaptive finite-time anti-saturated guaranteed control method.

Close-range proximity control with a tumbling target
In this simulation example, the chaser and target are in orbit around the earth, and the initial relative distance r is 0.3 km. Initial

Table. Initial orbital elements.

Initial orbit elements	Chaser	Target
Semi-major axis (km)	7,999.961	7,999.971
Eccentricity	0.01	0.01
Inclination (deg)	50	50
Right ascension of ascending node (deg)	10	10
Argument of perigee (deg)	29.99	29.98
True anomaly (deg)	111.082	111.092

orbit elements of the 2 spacecraft are presented in Table. The desired final relative distance r_d is set as 0.02 km. Initial quaternions of the chaser and target are $\boldsymbol{\varrho}_c = [-0.33, -0.22, -0.22, 0.89]^\top$ and $\boldsymbol{\varrho}_t = [-0.31, 0.55, -0.32, 0.71]^\top$, respectively. Inertia matrix of
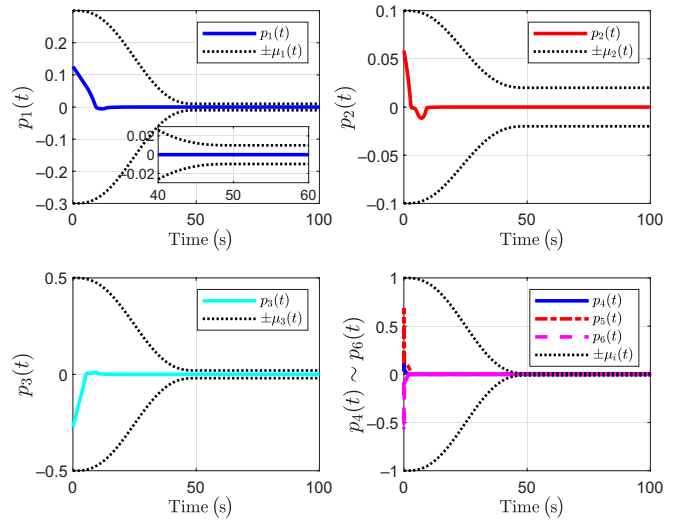
Fig. 3. Auxiliary state variable **p** under the proposed performance functions (Close-range proximity control with a tumbling target).
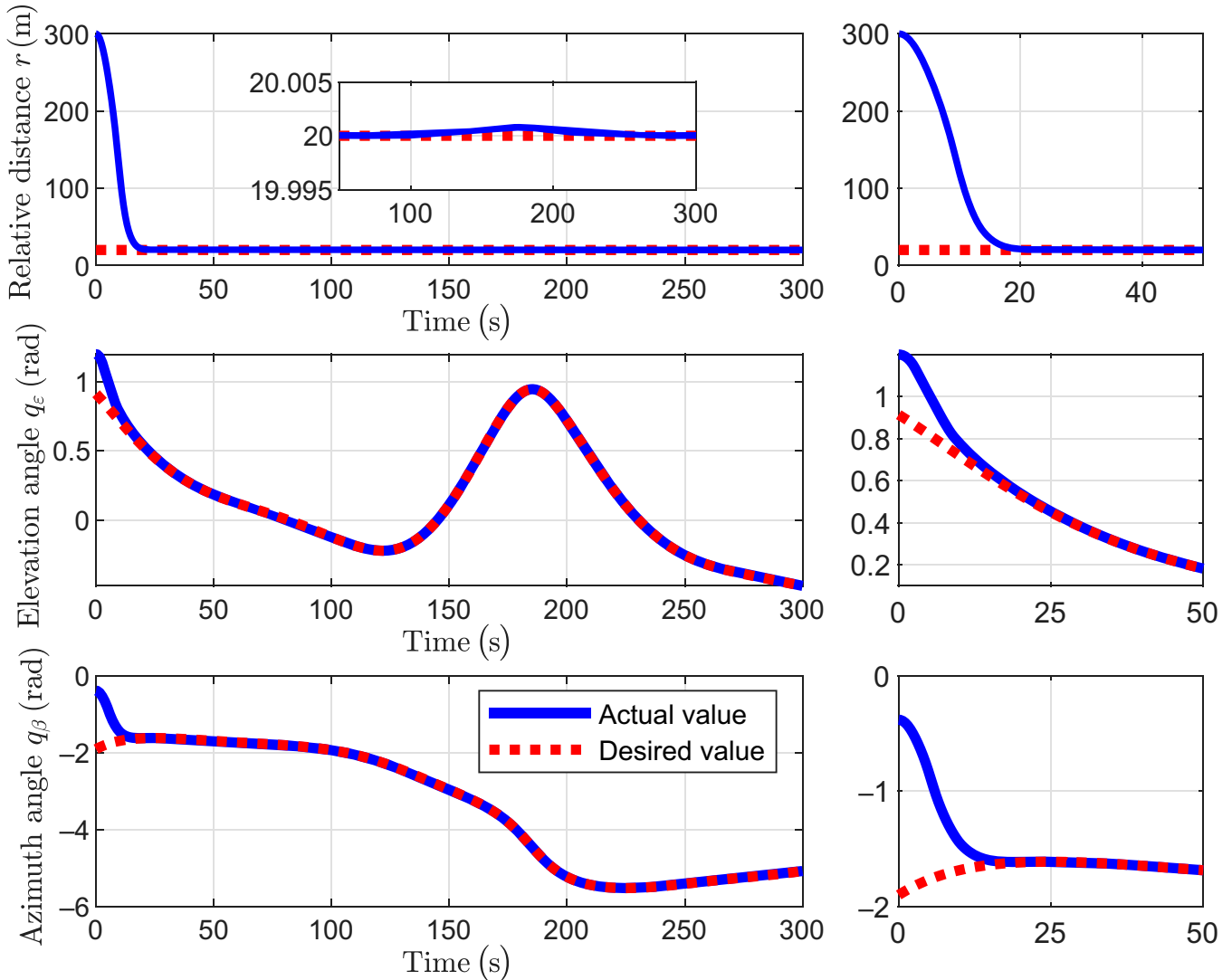
Fig. 4. LOS states tracking their desired trajectories (Close-range proximity control with a tumbling target).
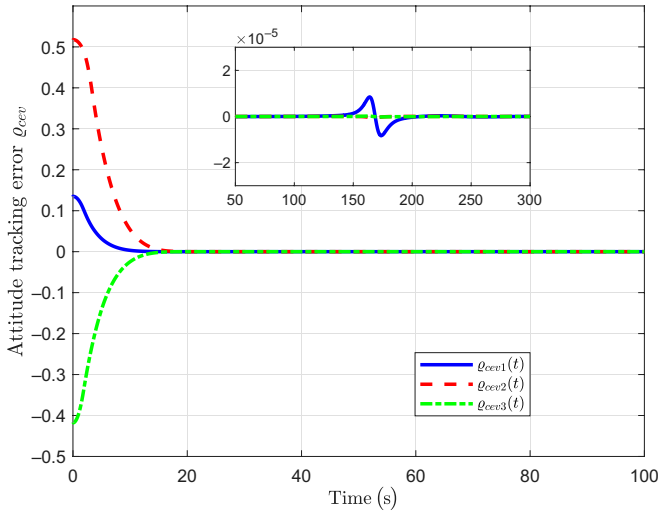
Fig. 5. Attitude quaternion error $\boldsymbol{\varrho}_{cev}$ (Close-range proximity control with a tumbling target).

the chaser is designed as $\boldsymbol{J}_c = \text{diag}\{100/6, 100/6, 100/6\}$, which is inaccessible to the controller. Unit vector of the feature point in the chaser's body-fixed coordinate is assumed as $\boldsymbol{n}_b = [1, 0, 0]^\top$. During the close-range proximity process, the direction of the solar ray in the inertial frame is assumed to remain unchanged and set as $\boldsymbol{\zeta} = \left[\sqrt{2}/2, -\sqrt{2}/2, 0\right]^\top$. In this example, the considered target has no active control forces or torques, and is tumbling with a initial angular velocity $\boldsymbol{\omega}_t = [1.5, 1.0, 1.2]^\top$ deg/s.

For the novel appointed-time convergent performance function in Eq. 17, the relative distance r is firstly nondimensionalized as $\bar{r} = r/(0.5\text{km})$ and the elevation and azimuth angles are specified in radians for the same order of magnitude. The reference points are designed as $\boldsymbol{y}_0 = \boldsymbol{y}_1 = \boldsymbol{y}_2 = [0.3, 0.1, 0.5, 1, 1, 1]^\top$, $\boldsymbol{y}_3 = 0.5\boldsymbol{y}_0$, $\boldsymbol{y}_4 = \boldsymbol{y}_5 = \boldsymbol{y}_6 = [0.01, 0.02, 0.02, 0.01, 0.01, 0.01]^\top$. The appointed time T_a for each dimension is similarly designed as $T_a = 100$ s. According to Corollary, the performance function $\boldsymbol{\mu}(t) = [\mu_1(t), \cdots, \mu_6(t)]^\top$ satisfies $\boldsymbol{\mu}(0) = \boldsymbol{y}_0$, and $\boldsymbol{\mu}(t) = \boldsymbol{y}_6$ for all $t \geq T_a$.

Parameters of the proposed controller (Eq. 25) are designed as $\boldsymbol{k} = \text{diag}\{300, 300, 300, 200, 200, 200\}$, $\boldsymbol{\lambda} = \text{diag}\{0.2, 0.2, 0.2, 0.2, 0.2, 0.2\}$, $\gamma = 0.8$ and $\delta = 1$, $\kappa_1 = \kappa_2 = 0.05$, $\kappa_3 = 0.1$. The orbit
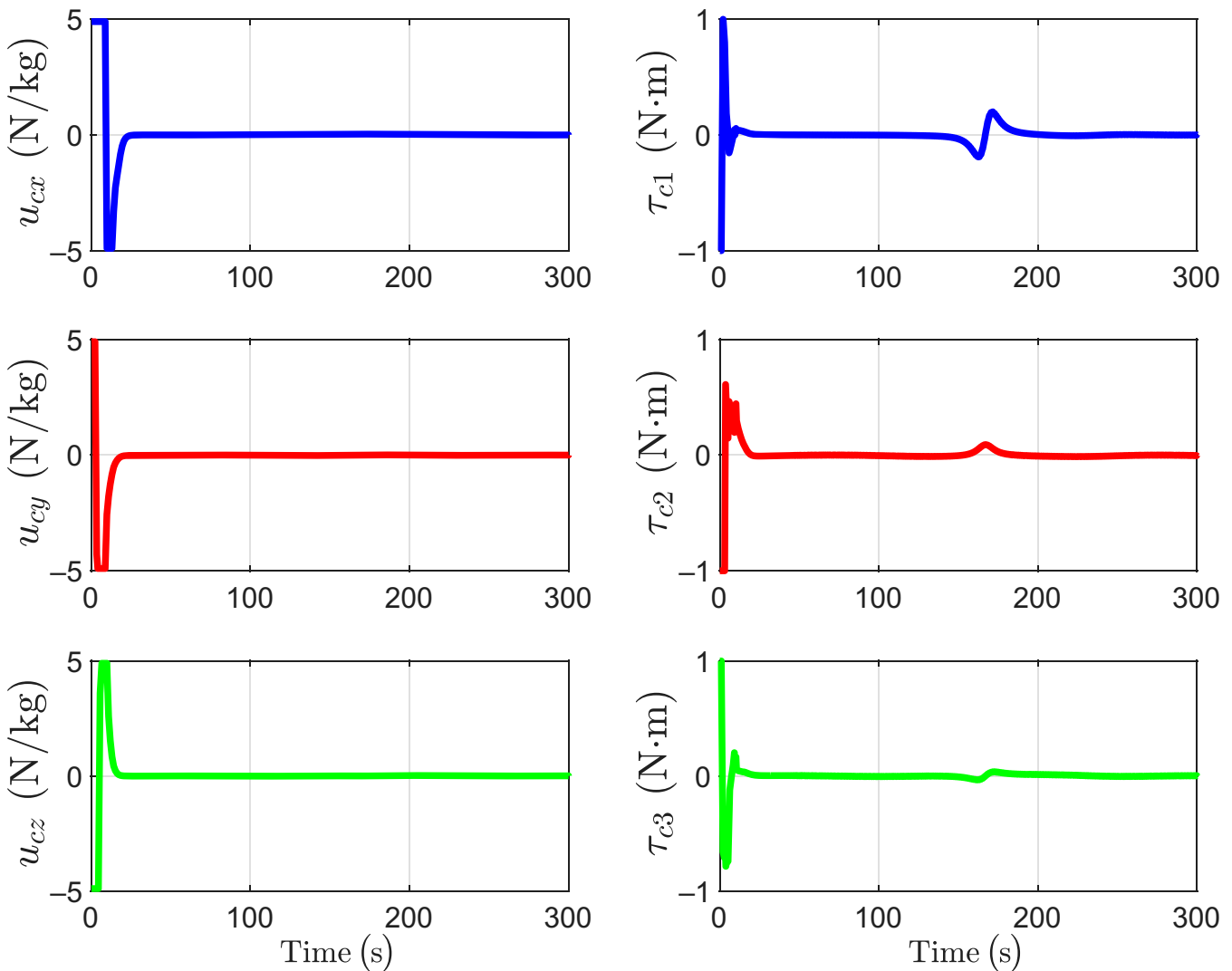

Fig. 6. Control inputs $\boldsymbol{u}_c$ and $\boldsymbol{\tau}_c$ (Close-range proximity control with a tumbling target).

and attitude control saturation limits are given as 4.9 N/kg and 1.0 N·m. The corresponding simulation results are presented in Figs. 3 to 7.

The constructed auxiliary state variable $p(t)$ is presented in Fig. 3, together with the corresponding appointed-time convergent performance function $\mu(t)$. Apparently, p is steered to a small neighbourhood around origin with guaranteed prescribed performance within appointed time instant T_a. The LOS states r, q_ϵ and q_β and their desired trajectories are given in Fig. 4. One can obtain that the LOS states can reach the desired trajectories before $T_a = 50$ s and accurately track them during the rendezvous process. Fig. 5 presents the tracking process of the attitude, and the same conclusion as the LOS states can be drawn. The orbit and attitude control inputs are presented in Fig. 6. The input saturation problem occurs at the beginning due to the big initial state errors. However, due to the novel appointed-time performance function with initial zero derivative and the proposed adaptive anti-saturation controller, the tracking control system is always stable and the influence of the saturation is reduced by the adaptive projection rule. The whole proximity and tracking process is presented in Fig. 7
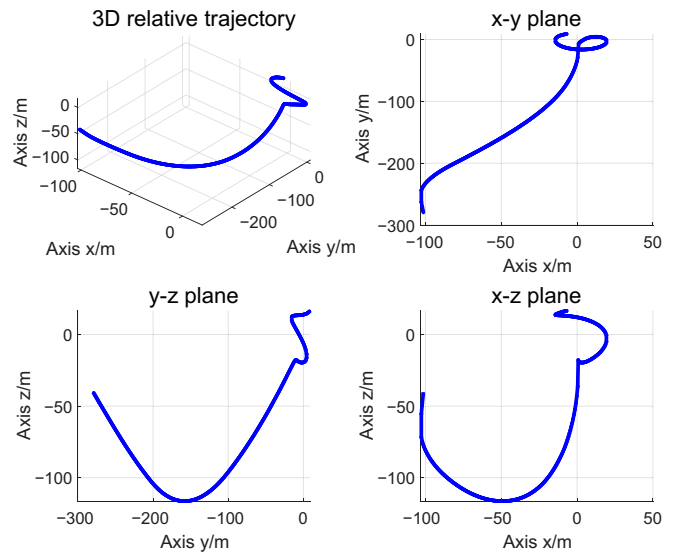
Fig. 7. 3D proximity trajectory (Close-range proximity control with a tumbling target).
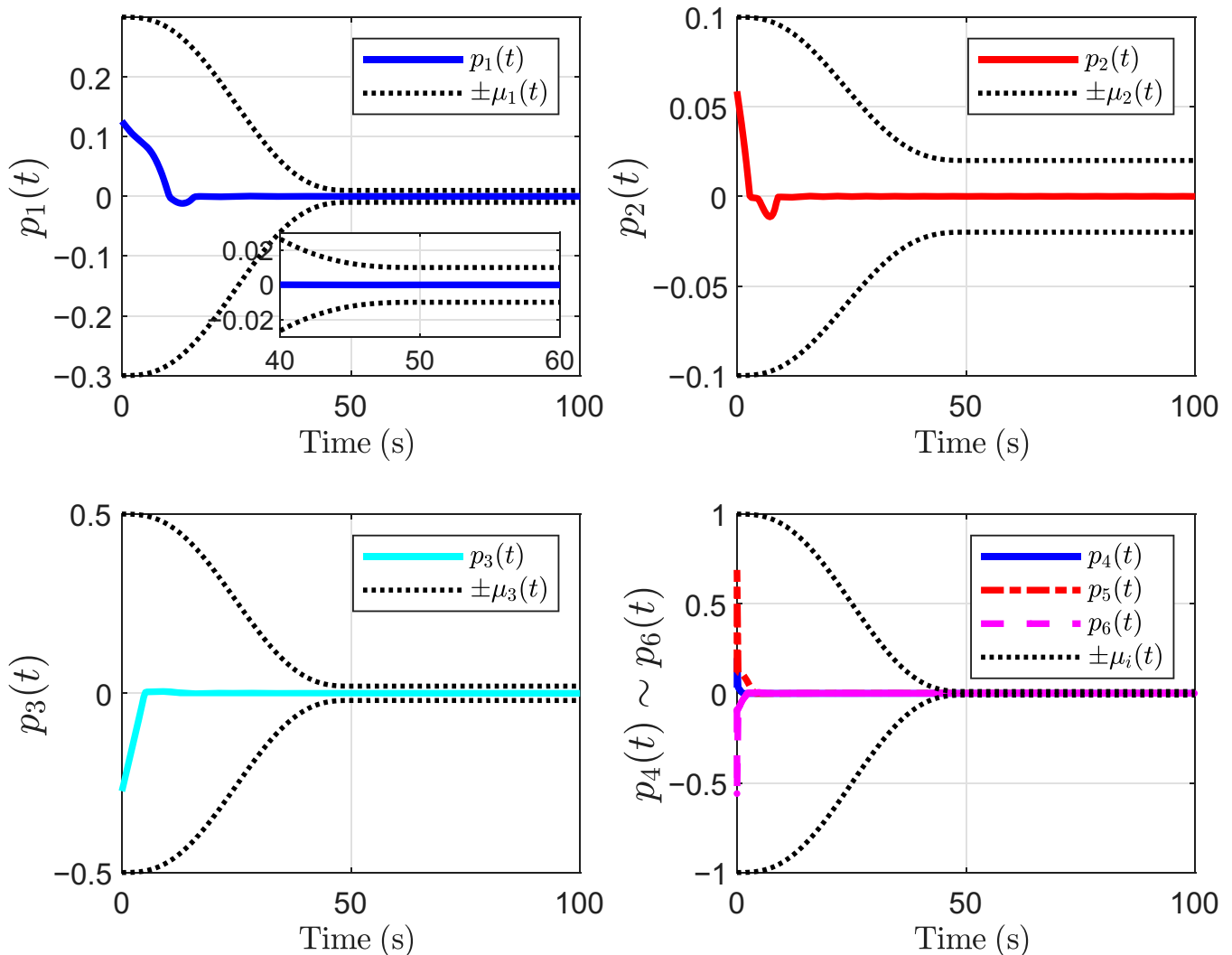
Fig. 8. Auxiliary state variable p under the proposed performance functions (Close-range proximity control with a tumbling and maneuvering target).
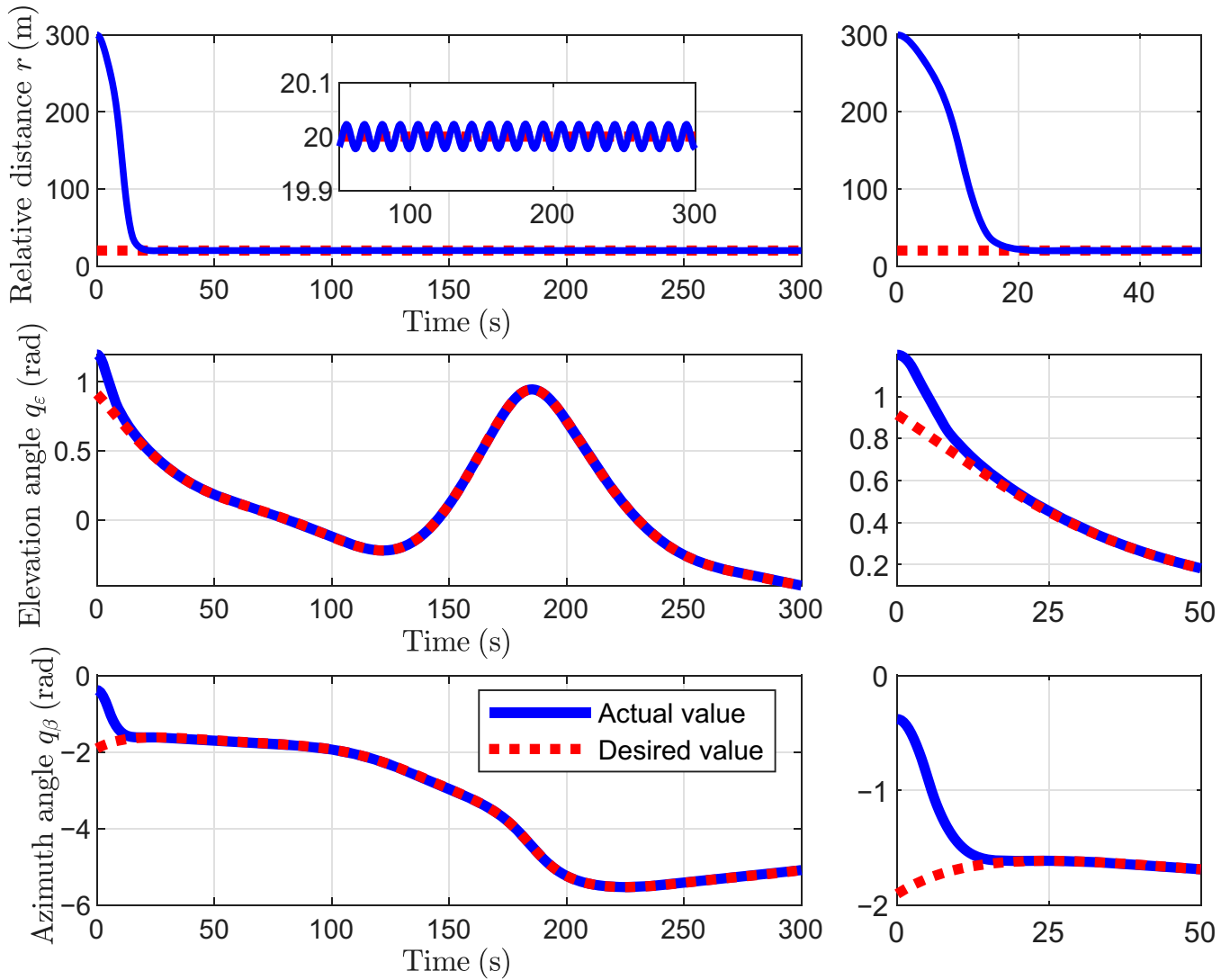
Fig. 9. LOS states tracking their desired trajectories (Close-range proximity control with a tumbling and maneuvering target).
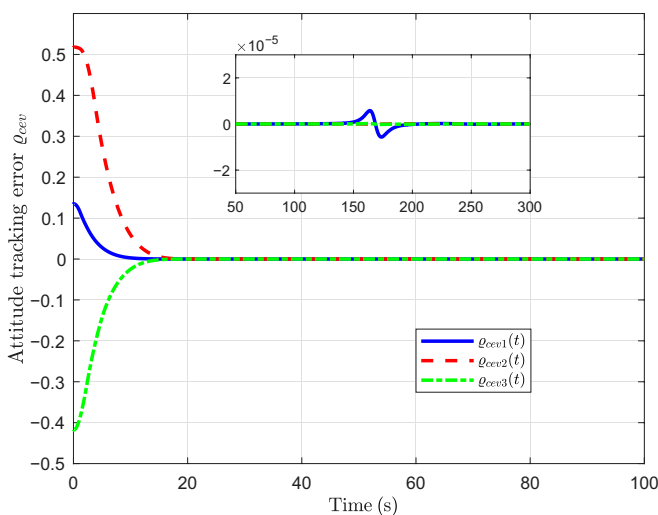

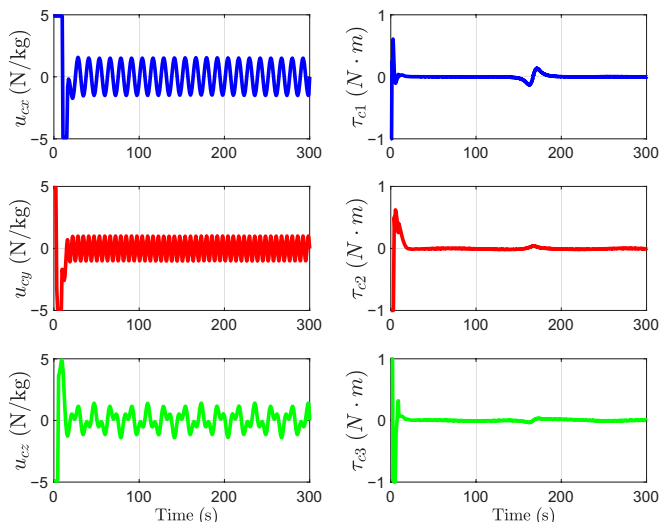**Fig. 10.** Attitude quaternion error ϱ_{cev} (Close-range proximity control with a tumbling and maneuvering target).

Fig. 11. Control inputs $\boldsymbol{u}_c$ and $\boldsymbol{\tau}_c$ (Close-range proximity control with a tumbling and maneuvering target).
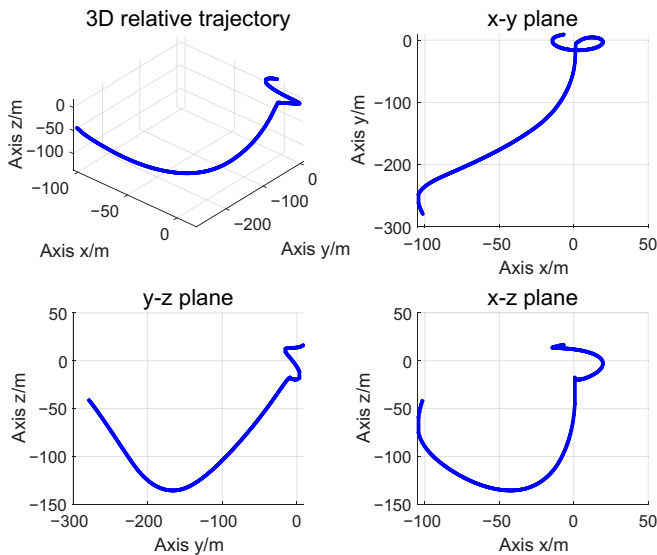
Fig. 12. 3D Proximity trajectory (Close-range proximity control with a tumbling target).

with the origin of coordinate fixed on the target. It is shown that the chaser can move along with the tumbling target and stay relatively still with the target, thus the proximity and docking mission is well realized.

Close-range proximity control with a tumbling and maneuvering target

In this simulation example, the initial system states, parameters, as well as the control parameters are selected the same with Close-range proximity control with a tumbling target, except for non-cooperative acceleration caused by the target. The acceleration a_t is designed as $a_t = [1.5 \sin(0.5t), -1.0 \cos(1.0 t), 0.8 \sin(0.3t) + 0.6 \sin(0.7t)]^\top$ N/kg, which means that the target is not only tumbling, but has large unknown maneuvers during the close-range proximity process. The considered example puts forward pretty high request to the robustness of the control system. The corresponding simulation results of this example are presented in Figs. 8 to 12.

The constructed auxiliary state variable $p(t)$ and its performance function $\mu(t)$ is presented in Fig. 8. The convergent process of $p(t)$ under $\mu(t)$ is basically the same as Fig. 3, which indicates that the proposed control method has strong robustness against the large non-cooperative maneuver a_t. The LOS states r, q_ϵ and q_β and their desired trajectories are given in Fig. 9. The dynamic performance of the tracking system is not influenced by the non-cooperative maneuver, while the steady-state error of $r(t)$ is obviously increased. It is noteworthy that the increased steady-state error is still within the prescribed stable region, and can be reduced by decreasing the prescribed value. There is not much change of the attitude tracking error in Fig. 10, as the attitude control system is not changed. The robustness of the proposed method against unknown non-cooperative maneuver can be viewed in Fig. 11, as the unknown maneuver is compensated by the control inputs. Finally, the whole proximity and tracking process is also presented in Fig. 12.

Conclusion

This paper has proposed a brand-new anti-saturated guaranteed performance control method for the close-range proximity

operations with a non-cooperative tumbling target. An appointed-time convergent performance function has been design with initial zero derivative based on Bézier curve. Moreover, an anti-saturated pose tracking controller has been constructed to realize the performance function. Simulation examples show that the constructed auxiliary states are appointed-time stable within the designed performance functions and the proximity and docking mission is well realized even with the maneuvering non-cooperative space target.

For future work, more non-cooperative properties of the target can be considered, e.g. the unavailable or inaccurate relative motion states. Furthermore, as there may exist solar panels and manipulators around the main body of the target, the obstacle avoidance rendezvous control problem is worth investigating to provide a safe rendezvous trajectory for the chaser spacecraft.

Acknowledgments

Data Availability

The data are available from the authors upon a reasonable request.

References

1. Flores-Abad A, Ma O, Pham K, Ulrich S. A review of space robotics technologies for on-orbit servicing. *Prog Aerosp Sci*. 2014;68:1–26.

2. Liu Y, Jiang Y, Li H. Analytical propagation of space debris density for collisions near sun-synchronous orbits. *Space Sci Technol*. 2022;2022:Article 9825763.

3. Cao K, Li S, She Y, Biggs JD, Liu Y, Bian L. Dynamics and on-orbit assembly strategies for an orb-shaped solar array. *Acta Astronaut*. 2021;178:881–893.

4. Li D, Zhong L, Zhu W, Xu Z, Tang Q, Zhan W. A survey of space robotic technologies for on-orbit assembly. *Space Sci Technol*. 2022;2022:Article 9849170.

5. Pan H, Cao S, Wu H, Jing Z, Dun X. Non-cooperative space target relative pose estimation via truncated least squares and semi-definite programming. *Flight Control and Detection*. 2022;5(4):50–56.

6. Luo Y, Zhang J, Tang G. Survey of orbital dynamics and control of space rendezvous. *Chin J Aeronaut*. 2014;27(1):1–11.

7. Qu Q, Liu K, Wang W, Lü J. Spacecraft proximity maneuvering and rendezvous with collision avoidance based on reinforcement learning. *IEEE Trans Aerosp Electron Syst*. 2022;58(6):5823–5834.

8. Gao H, Yang X, Shi P. Multi-objective robust H_∞ control of spacecraft rendezvous. *IEEE Trans Control Syst Technol*. 2009;17(4):794–802.

9. Gavilan F, Vazquez R, Camacho EF. Chance-constrained model predictive control for spacecraft rendezvous with disturbance estimation. *Control Eng Pract*. 2012;20(2):111–122.

10. Dong K, Luo J, Dang Z, Wei L. Tube-based robust output feedback model predictive control for autonomous rendezvous and docking with a tumbling target. *Adv Space Res*. 2020;65(4):1158–1181.

11. Capello E, Punta E, Dabbene F, Guglieri G, Tempo R. Sliding-mode control strategies for rendezvous and docking maneuvers. *J Guid Control Dyn*. 2017;40(6):1481–1487.

12. Hu Q, Chen W, Zhang Y. Concurrent proximity control of servicing spacecraft with an uncontrolled target. *IEEE ASME Trans Mechatron*. 2019;24(6):2815–2826.

13. Gong B, Ma Y, Zhang W, Li S, Li X. Deep-neural-network-based angles-only relative orbit determination for space non-cooperative target. *Acta Astronaut*. 2023;204:552–567.

14. Gong B, Wang S, Li S, Li X. Review of space relative navigation based on angles-only measurements. *Astrodynamics*. 2023;7(2):131–152.

15. Kim BS, Calise AJ, Sattigeri RJ. Adaptive, integrated guidance and control design for line-of-sight-based formation flight. *J Guid Control Dyn*. 2007;30(5):1386–1399.

16. Jiang B, Hu Q, Friswell MI. Fixed-time rendezvous control of spacecraft with a tumbling target under loss of actuator effectiveness. *IEEE Trans Aerosp Electron Syst*. 2016;52(4):1576–1586.

17. Zhang K, Duan G, Ma M. Adaptive sliding-mode control for spacecraft relative position tracking with maneuvering target. *Int J Robust Nonlinear Control*. 2018;28(18):5786–5810.

18. Sun L, Jiang J. Saturated adaptive relative motion coordination of docking ports in space close-range rendezvous. *IEEE Trans Aerosp Electron Syst*. 2020;56(6):4889–4898.

19. Hu Q, Liu Y, Zhang Y. Control of non-cooperative spacecraft in final phase proximity operations under input constraints. *Control Eng Pract*. 2019;87:83–96.

20. Zhang K, Duan G. Passivity-based adaptive tracking control of spacecraft line-of-sight relative motion with thrust saturation. *J Franklin Inst*. 2021;358(13):6408–6432.

21. Bechlioulis CP, Rovithakis GA. Robust adaptive control of feedback linearizable MIMO nonlinear systems with prescribed performance. *IEEE Trans Autom Control*. 2008;53(9):2090–2099.

22. Wang M, Yang A. Dynamic learning from adaptive neural control of robot manipulators with prescribed performance. *IEEE Trans Syst Man Cybern Syst*. 2017;47(8):2244–2255.

23. Dai S-L, He S, Lin H, Wang C. Platoon formation control with prescribed performance guarantees for USVs. *IEEE Trans Ind Electron*. 2018;65(5):4237–4246.

24. Wei C, Wu X, Xiao B, Wu J, Zhang C. Adaptive leader-following performance guaranteed formation control for multiple spacecraft with collision avoidance and connectivity assurance. *Aerosp Sci Technol*. 2022;120:Article 107266.

25. Li Y, Tong S. Adaptive fuzzy control with prescribed performance for block-triangular-structured nonlinear systems. *IEEE Trans Fuzzy Syst*. 2018;26(3):1153–1163.

26. Na J, Huang Y, Wu X, Gao G, Herrmann G, Jiang JZ. Active adaptive estimation and control for vehicle suspensions with prescribed performance. *IEEE Trans Control Syst Technol*. 2018;26(6):2063–2077.

27. Wei C, Luo J, Dai H, Duan G. Learning-based adaptive attitude control of spacecraft formation with guaranteed prescribed performance. *IEEE Trans Cybern*. 2019;49(11):4004–4016.

28. Hu Y, Geng Y, Wu B, Wang D. Model-free prescribed performance control for spacecraft attitude tracking. *IEEE Trans Control Syst Technol*. 2021;29(1):165–179.

29. Wei C, Xiong Y, Chen Q, Xu D. On adaptive attitude tracking control of spacecraft: A reinforcement learning based gain tuning way with guaranteed performance. *Adv Space Res*. 2023;71(11):4534–4548.

30. Shao X, Hu Q, Shi Y. Adaptive pose control for spacecraft proximity operations with prescribed performance under spatial motion constraints. *IEEE Trans Control Syst Technol*. 2021;29(4):1405–1419.

31. Liu Y, Liu X, Jing Y. Adaptive neural networks finite-time tracking control for non-strict feedback systems via prescribed performance. *Inf Sci*. 2018;468:29–46.

32. Liu M, Shao X, Ma G. Appointed-time fault-tolerant attitude tracking control of spacecraft with double-level guaranteed performance bounds. *Aerosp Sci Technol*. 2019;92:337–346.

33. Zhang R, Xu B, Zhao W. Finite-time prescribed performance control of MEMS gyroscopes. *Nonlinear Dyn*. 2020;101:2223–2234.

34. Wei C, Gui M, Zhang C, Liao Y, Dai M-Z, Luo B. Adaptive appointed-time consensus control of networked Euler-Lagrange systems with connectivity preservation. *IEEE Trans Cybern*. 2022;52(11):12379–12392.

35. Zhang Y, Wu G, Yang X, Song S. Appointed-time prescribed performance control for 6-dof spacecraft rendezvous and docking operations under input saturation. *Aerosp Sci Technol*. 2022;128:Article 107744.

36. Wei C, Chen Q, Liu J, Yin Z, Luo J. An overview of prescribed performance control and its application to spacecraft attitude system. *Proc Inst Mech Eng I*. 2021;235(4):435–447.

37. Zhang B, Jiang L, Bai J. Velocity-free prescribed performance control for spacecraft hovering over an asteroid with input saturation. *J Franklin Inst*. 2020;357(11):6471–6497.

38. Shin H-S, Tsourdos A, Li K-B. A new three-dimensional sliding mode guidance law variation with finite time convergence. *IEEE Trans Aerosp Electron Syst*. 2017;53(5):2221–2232.

39. Hu Q, Shao X, Chen W-H. Robust fault-tolerant tracking control for spacecraft proximity operations using time-varying sliding mode. *IEEE Trans Aerosp Electron Syst*. 2017;54(1):2–17.

40. Zhang X, Li S, Wang B, Wang B. Attitude stabilization of spacecraft using variable step-size pulse-width-modulated thrusters. *J Guid Control Dyn*. 2022;45(2):376–384.

41. Wang L, Chai T, Zhai L. Neural-network-based terminal sliding-mode control of robotic manipulators including actuator dynamics. *IEEE Trans Ind Electron*. 2009;56(9):3296–3304.

42. Zou Y, Zheng Z. A robust adaptive RBFNN augmenting backstepping control approach for a model-scaled helicopter. *IEEE Trans Control Syst Technol*. 2015;23(6):2344–2352.

43. Jolly K, Kumar RS, Vijayakumar R. A Bezier curve based path planning in a multi-agent robot soccer system without violating the acceleration limits. *Robot Auton Syst*. 2009;57(1):23–33.

44. Yin Z, Suleman A, Luo J, Wei C. Appointed-time prescribed performance attitude tracking control via double performance functions. *Aerosp Sci Technol*. 2019;93:Article 105337.

45. Bhat SP, Bernstein DS. Finite-time stability of continuous autonomous systems. *SIAM J Control Optim*. 2000;38(3):751–766.